

# Modeling the cross-shore evolution of asymmetry and skewness of surface gravity waves propagating over a natural intertidal sandbar

*Joost Brinkkemper (3564932)*

MSc Thesis

*Supervisor: Dr. B.G. Ruessink*

Department of Physical Geography

Faculty of Geosciences

Utrecht University

The Netherlands



Modeling the cross-shore evolution of asymmetry and skewness of surface gravity waves  
propagating over an intertidal sandbar

Joost Brinkkemper (3564932)

MSc Thesis – February 11, 2013



Department of Physical Geography  
Faculty of Geosciences  
Utrecht University

Supervisor:  
Dr. B.G. Ruessink





# Contents

<b>Acknowledgements</b>	<b>2</b>
<b>1 Introduction</b>	<b>3</b>
<b>2 Background information</b>	<b>5</b>
2.1 Nonlinear effects in shoaling waves . . . . .	5
2.2 Skewness and asymmetry . . . . .	5
2.3 Spectral and bispectral analyses . . . . .	6
2.4 Modeling waves in the nearshore zone . . . . .	7
2.5 Problem description and research focus . . . . .	9
<b>3 Methodology</b>	<b>10</b>
3.1 SWASH model . . . . .	10
3.2 Field campaign . . . . .	11
3.2.1 Introduction to area . . . . .	11
3.2.2 Instrumentation . . . . .	11
3.2.3 Hydro- and morphodynamics . . . . .	12
3.2.4 Data analysis . . . . .	13
3.3 Data selection . . . . .	16
3.4 Model implementation . . . . .	19
3.5 Sensitivity analysis . . . . .	20
3.5.1 Spatial resolution . . . . .	20
3.5.2 Bottom friction . . . . .	20
3.5.3 Offshore boundary forcing . . . . .	21
3.5.4 Hydrostatic and non-hydrostatic pressure . . . . .	22
<b>4 Results</b>	<b>24</b>
4.1 Breaking . . . . .	24
4.2 High frequency wave height . . . . .	24
4.3 Wave energy spectra . . . . .	29
4.4 Skewness and Asymmetry . . . . .	34
<b>5 Conclusions</b>	<b>39</b>
<b>6 Discussion and Recommendations</b>	<b>39</b>
<b>References</b>	<b>41</b>
<b>A Offshore boundary forcing</b>	<b>43</b>

## Acknowledgements

First of all I would like to thank my supervisor, Gerben Ruessink for his guidance, motivation and the sharing of his invaluable knowledge and experience. Thanks to Marijn en Stefan for making the field campaign a very pleasant period and for all the fruitful discussion during the campaign and afterwards. Also I want to express my gratitude to my parents for their unconditional support throughout my study.

# 1 Introduction

In the nearshore zone, broadly defined as the region along a coast with waterdepth  $< 10\text{m}$ , surface gravity waves are the most important source of energy. This energy is mostly dissipated by wave breaking and converted into nearshore currents, turbulence and sediment transport (Masselink and Hughes, 2003). Knowledge about the transformation of waves and dissipation of wave energy in the nearshore zone is essential for understanding the dynamics of coastal morphology, as they are the driving forces of erosion and sedimentation.

The nearshore zone is divided in three sections, based on their hydrodynamics. From the seaward side these are: shoaling, surf and swash zone. Waves transform from sinusoidal (Figure 1a) to skewed (Figure 1b) in the shoaling zone; then the waves break and obtain a highly asymmetric shape (Figure 1c) to finally runup on the beach in the swash zone. Skewed waves are characterized by a high narrow crest and a broad shallow trough (Figure 1b), asymmetric waves by a forward leaning saw-tooth shape (Figure 1c). The skewness and asymmetry is reflected in the near-bed orbital velocity beneath the waves, resulting in onshore sediment transport. Skewness means higher flow velocities in onshore direction under the crest of the waves, which moves more coarse sediment towards the shore. Under waves with high asymmetry, the change from onshore to offshore flow is more gradual then from offshore to onshore, this gives particles moved in onshore direction more time to settle. Moreover, sediment stirred up from the bed by offshore flow is taken onshore due to the fast change in flow direction (Ruessink et al., 2011). This process contributes to beach accretion during mild energetic conditions.

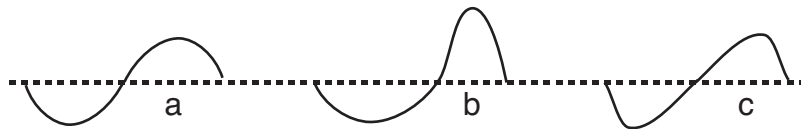


Figure 1: Waves with a (a) sinusoidal, (b) skewed and (c) asymmetric shape.

For this reason, including wave shape in wave models is essential to predict the morphodynamics in the nearshore zone. Two different approaches exist to include wave shape in models, the phase-averaged approach and the phase-resolving approach. With the phase-averaged approach, wave skewness and asymmetry is included based on parameterizations, see Ruessink et al. (2012) and references therein. More advanced wave models, for example the ones based on the Reynolds-Averaged Navier Stokes (RANS), Boussinesq or nonlinear shallow water (NLSW) equations, are phase-resolving. These models are computationally demanding and thus not very suitable for modeling with the typical time scale of morphodynamics.

In the past years, SWASH (Simulating WAVes till SHore) has been developed, a non-hydrostatic wave model that solves the NLSW equations (Zijlema et al., 2011). This model is relatively efficient, and no coefficients or additional models are needed for the initiation of wave breaking and wave-wave and wave-current interaction in shallow water. This makes the SWASH model, besides its user-friendliness, a very promising tool to predict hydrodynamics in the nearshore zone. Zijlema et al. (2011) show the performance of the model for a wide range of laboratory cases, but a validation of the SWASH model with field measurements is lacking until now.

This research presents a validation of the SWASH model for field measurements, taken during a measurement campaign from October 27 until November 2, 2011 at the Dutch coast, near the town of Egmond aan Zee. During this campaign, hydrodynamics and sediment concentrations were measured in a cross-shore transect over an intertidal sandbar, the beach morphology was mapped and video images were taken to extract wave breaking location and runup dynamics. The focus of the field validation is on wave shape evolution and wave breaking, because of their importance for sediment transport.

This report describes all aspects of the research, starting with a literature review on nearshore

hydrodynamics and wave modeling in Section 2. This section ends with a synthesis of the literature, a problem description and the research questions (Section 2.5). The questions are followed by the methodology in Section 3, describing the measurement campaign and the SWASH model in more detail. The model sensitivity to spatial resolution and friction, and the results are presented in Section 4, followed by the conclusions (Section 5) and recommendations (Section 6) for further research.

## 2 Background information

### 2.1 Nonlinear effects in shoaling waves

Water particles under a propagating wave in deep water follow an almost circular path, under the crest in the direction of wave propagation and under the trough in the opposite direction (Figure 2). The velocity of the particles decreases with depth. The term deep water is used when the particle motion underneath a wave does not reach the seabed. Water is considered deep when  $h/L > 0.5$ , in which  $h$  is the water depth and  $L$  is the wave length (Masselink and Hughes, 2003; van Rijn, 1990). If  $h/L < 0.5$  surface water waves enter intermediate water and the particle motion is influenced by the sea bed. As the water depth decreases, the path of the particles underneath the waves becomes more elliptic towards the bed, resulting in horizontal particle movement under surface waves in shallow water (Figure 2). Waves not only change the shape of the particle movement from deep to intermediate water, they also refract, increase in wave amplitude, and shorten their length. These linear processes are well understood and can be described with linear (or Airy) wave theory.

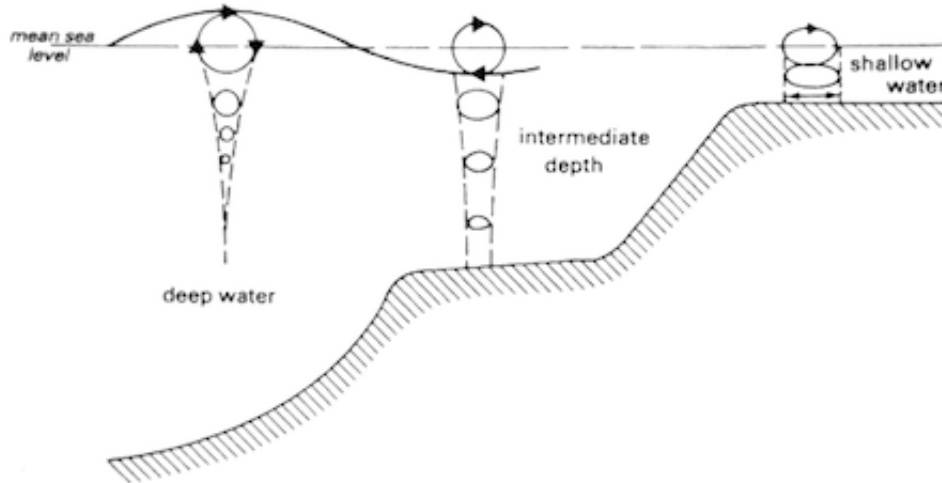


Figure 2: Orbital wave motions in deep, intermediate and shallow water according to linear wave theory (van Rijn, 1990)

Linear wave theory describe waves when the importance of nonlinear terms is negligible, which is the case for deep water or when  $H/h$  and  $H/L$  are small (van Rijn, 1990). When waves propagate into shallower water, second-order Stokes theory is still able to take the nonlinearities due to wave shoaling into account. But when waves propagate into shallow water and their shape becomes asymmetrical in the vertical plane, this Stoke theory is no longer applicable. Comparing measured wave heights and linear shoaling theory in the nearshore zone for a small bottom slope ( $1.3^\circ$ ) between 10 and 3m depth results in a error in the predicted wave height under 20%, although it can be higher for particular frequency bands in the wave energy spectrum (Guza and Thornton, 1980). In the section shoreward of the 3m depth contour, the nonlinear effects become more dominant, with an increase towards the location of wave breaking. These results show the necessity to include nonlinear effects in wave propagation calculations.

### 2.2 Skewness and asymmetry

Due to nonlinear effects, the wave shape changes from nearly sinusoidal to skewed (vertical asymmetric), with a short and high wave crest and a long and flat wave trough, to a horizontal asymmetric shape with a forward leaning pitch (horizontal asymmetry and slope asymmetry) (Elgar and Guza, 1985). Figure 3 shows a typical wave profile for shallow waters, with definitions for horizontal, vertical and slope asymmetry. The definition for vertical asymmetry is often



used to describe the skewness of waves, with  $a_c/H = 0.5$  for zero skewness, increasing to  $a_c/H = 0.7 - 0.8$  at the location of wave breaking, after which the ratio decreases to 0.5 and the waves transform to a sawtooth shape (high asymmetry) towards the shore (Svendsen, 2006).

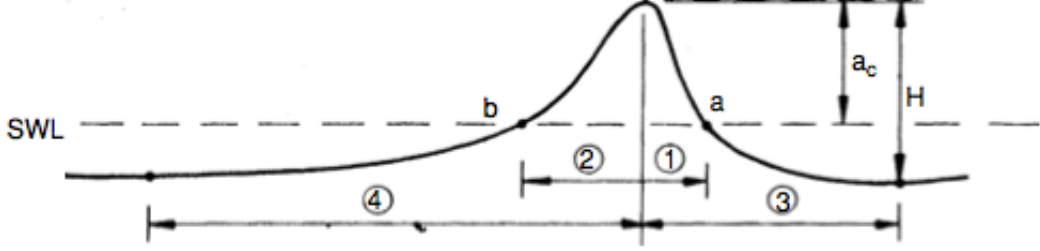


Figure 3: Definition of the wave profile asymmetry terms by Sorensen (2005). Vertical asymmetry =  $a_c/H$ , slope asymmetry =  $0.5(\text{slope } a + \text{slope } b)$ , horizontal asymmetry = distance 1/distance 2 or distance 3/distance 4.

Skewness and asymmetry are more commonly defined as:

$$Sk = \frac{\langle \eta^3 \rangle}{\langle \eta^2 \rangle^{3/2}} \quad (1)$$

$$As = \frac{\langle H(\eta)^3 \rangle}{\langle \eta^2 \rangle^{3/2}}, \quad (2)$$

in which  $\eta$  is the zero-mean wave surface elevation and  $H$  is the Hilbert transform. The angle brackets indicate averaging over many waves.  $Sk$  and  $As$  are often related to the Ursell number, where the Ursell number is defined as:

$$Ur = aL^2/h^3, \quad (3)$$

with  $a = 0.5H_{m0}$ . For small Ursell numbers ( $Ur \ll 0.1$ ),  $Sk$  and  $As$  approach zero (sinusoidal waves);  $Sk$  reaches a maximum value when  $Ur \approx 1$ , and  $As$  is still small (skewed waves). For larger Ursell numbers,  $Sk \rightarrow 0$  and  $As \rightarrow -2.86$  (Doering and Bowen, 1995). These values for maximum Ursell numbers are typical for the inner surf zone, where waves have a sawtooth-like shape.

The transformation of the wave shape also leads to flow velocity skewness and asymmetry. The velocity skewness is comparable with the shape of the waves, i.e. high velocity with short duration under the crest, and low velocity with a long duration under the trough. This difference is important for the sediment transport by wave motion, as the high velocities under the crest are much more capable of moving large sediments. This mechanism was first observed by Cornish (1898) and demonstrated in detail by Ribberink et al. (2008) under controlled laboratory conditions. Velocity asymmetry can also result in a net onshore transport of sediment. This is explained by the smooth change in flow direction from onshore to offshore, which gives sediments more time to settle, compared to the sudden change from offshore to onshore, where sediments are stirred up during peaks in offshore velocity and are transported onshore because of the sudden change in flow direction (Ruessink et al., 2011).

### 2.3 Spectral and bispectral analyses

To analyze an irregular wave field, water surface measurements are often visualized in a wave energy spectrum, which is a plot of the spectral density ( $m^2/Hz$ ) versus wave frequency ( $Hz$ ). Distinction between the wave frequencies that exist in a wave field can be made using the spectrum. With the wave energy spectrum, also the origin of wave asymmetry and skewness can be explained and quantified.

Wave energy spectra transform when propagating into shallow water. This is explained by interaction between wave frequency components, resulting in an increase of energy at the higher and lower frequencies. Interaction of components with frequency  $f_1$  and  $f_2$  result in energy transfer to frequency  $f_3$  by summation ( $f_1 + f_2 = f_3$ ) or subtraction ( $f_1 - f_2 = f_3$ ). Self wave-wave interactions of the primary frequency result in the growth of energy at twice the primary frequency.

Changes in the wave energy spectrum due to nonlinear wave coupling can be distinguished from independent non-coupled waves with the bispectrum. The bispectrum is defined as (Kim and Powers, 1979)

$$B(\omega_1, \omega_2) = E[A_{\omega_1} A_{\omega_2} A_{\omega_1 + \omega_2}^*], \quad (4)$$

in which  $\omega$  is the radian frequency,  $A$  is a complex Fourier coefficient and  $E[\ ]$  is called expected-value operator. If the phases of the wave components,  $\omega_1$ ,  $\omega_2$  and  $\omega_1 + \omega_2$ , are independent and random, the bispectrum takes on a zero value, due to the averaging in the formula. If the components are nonlinearly coupled, phase coherence exist and as a result the bispectrum is not zero after the statistical averaging. The normalized magnitude and phase of the bispectrum are the bicoherence and biphas respectively, which are defined respectively as (Kim and Powers, 1979)

$$b^2(\omega_1, \omega_2) = \frac{|B(\omega_1, \omega_2)|^2}{E[|A_{\omega_1} A_{\omega_2}|^2] E[|A_{\omega_1 + \omega_2}|^2]}, \quad (5)$$

$$\beta(\omega_1, \omega_2) = \arctan \left[ \frac{\text{Im}\{B(\omega_1, \omega_2)\}}{\text{Re}\{B(\omega_1, \omega_2)\}} \right]. \quad (6)$$

$\text{Im}$  and  $\text{Re}$  in Equation 6 represent the imaginary and real part of the bispectrum respectively. The bicoherence takes a value between 0 for random phase relationships, and 1 for maximum phase coupling, which means that wave components have a constant relative phase. The imaginary and real parts of the bispectrum are related to the skewness and asymmetry of the waves respectively (Kim and Powers, 1979), which are calculated as:

$$\text{Skewness} = \left[ 12 \sum_n \sum_l \text{Re}\{B(\omega_n, \omega_l)\} + 6 \sum_n \text{Re}\{B(\omega_n, \omega_n)\} \right] / E[\eta^2]^{3/2}, \quad (7)$$

$$\text{Asymmetry} = \left[ 12 \sum_n \sum_l \text{Im}\{B(\omega_n, \omega_l)\} + 6 \sum_n \text{Im}\{B(\omega_n, \omega_n)\} \right] / E[\eta^2]^{3/2}. \quad (8)$$

The ratio between the imaginary and real part results in the biphas of the bispectrum (equation 6). For this reason the biphas can also be used as a measure for the wave shape.

The origin of asymmetry in waves is explained by the forward phase-shifting of the harmonic components relative to the primary, which causes the relative steepening of the wave front. Eventually this phase-shifting of the harmonics lead to a decrease in wave skewness and an increase in wave asymmetry (Elgar and Guza, 1985, 1986). The value of the biphas between a power spectral peak and its harmonics changes when waves are approaching a shoreline from around zero (nonlinear skewed wave) to a value of  $\beta = -\frac{1}{2}\pi$  for waves with a sawtooth shape in very shallow water (Elgar and Guza, 1985).

## 2.4 Modeling waves in the nearshore zone

In recent years, considerable effort has been made to improve models that can simulate wave propagation till shore. For an accurate simulation of the nonlinear evolution of waves in the shoaling- and surfzone, phase resolving models are needed. The two most used phase resolving models are Boussinesq (Madsen et al., 2002) and non-hydrostatic models (Casulli and Stelling,

1998), which both resolve the wave field on the timescale of individual waves. This timescale is needed to calculate the nonlinear wave interactions and frequency dispersion accurately.

The Boussinesq type models are based on the Boussinesq equations (Peregrine, 1967), which describe the propagation of nonbreaking waves in shallow water, including nonlinearity and dispersion. These equations are only valid when nonlinearity and frequency dispersion are weak and of the same order of magnitude. In very shallow water nonlinearity is more important than frequency dispersion and in deep water frequency dispersion is order one, making the Boussinesq equations only valid for the zone in between, in waters of intermediate depth.

Since the existence of Boussinesq models, many attempts have been made to extend the models towards the surf zone (see Svendsen (2006) for an overview). To do so, other equations including wave breaking and energy dissipation must be added for very shallow water. This can be done in many ways, but they always include empirical relations or dissipation coefficients for wave breaking. The need for such empirical calibrated criteria, to calculate when and where waves are breaking, is still the main limitation of the Boussinesq models (Musumeci et al., 2005).

The non-hydrostatic type models make use of the nonlinear shallow water (NLSW hereinafter) equations, which are given as (Svendsen, 2006):

$$\frac{\partial}{\partial t}\eta + \nabla_h(\tilde{u}(h + \eta)) = 0, \quad (9)$$

$$\frac{\partial}{\partial t}\tilde{u} + \tilde{u} \cdot \nabla_h \tilde{u} + g\nabla_h\eta = 0, \quad (10)$$

in which  $\tilde{u}$  is the depth averaged horizontal orbital velocity,  $g$  the gravitational acceleration,  $\nabla$  the gradient operator and  $\eta$  the deviation of the water level from the mean. These equations assume hydrostatic pressure, so are only valid for long waves shoreward of the breaking zone and for breaking and broken waves (steady bores) in the surf zone (Raubenheimer et al., 1996; van Rijn, 1990). When waves propagate according to those equations, each part of the wave will propagate with its own velocity, according to  $c = \sqrt{gh}$ . This means that the crest is propagating with a higher speed than the trough of a wave, which results in a steepening of the wave front (Figure 4). These equations are mass and momentum conservative and can also simulate discontinuities, such as hydraulic jumps and bores. Bores are simulated by waves with a vertical wave crest, of which the wave shape is balanced by turbulence, in this way energy dissipation in a wave bore is included in the equations.



Figure 4: Wave deformation according to the nonlinear shallow water equations (Svendsen, 2006)

To extend the NLSW equations to the pre-breaking zone, terms for non-hydrostatic pressure must be added. To understand the need of including non-hydrostatic pressure in the equations, the difference between hydrostatic and non-hydrostatic pressure is explained briefly. Hydrostatic pressure can be described as the weight of the fluid above a certain location when the fluid is at rest, which can be calculated as:

$$p = \rho g(h - z), \quad (11)$$

in which  $\rho$  is the water density and  $z$  is height above the bottom. When a fluid is in motion, the pressure deviates from the hydrostatic pressure as the vertical pressure gradient also depends

on vertical acceleration and friction. The fluid pressure is then represented by a summation of the hydrostatic pressure (related to the water depth) and the dynamic pressure (causing fluid particle acceleration). Casulli (1999) describes the decomposition of the pressure into a hydrostatic and a non-hydrostatic component to solve the NLSW equations for both components separately. This makes the equations also suitable for simulating the propagation of short nonlinear waves (i.e. frequency dispersion) in the shoaling zone.

Previously, non-hydrostatic models needed around 20 layers in the vertical direction to model wave transformation accurately, which made the Boussinesq type models much more efficient. As a result, in recent years the focus was on improving the Boussinesq type models. As mentioned, the main disadvantage of the Boussinesq equations is that they are only valid in the shoaling zone. Other equations are coupled to the Boussinesq equations in order to extend them to the surf zone, but criteria for the initiation of breaking and amount of energy dissipation are needed. The nonlinear shallow water equations are only valid for the surf zone, but when non-hydrostatic pressure is added to these equations, the equations are also applicable in the shoaling zone.

Recently, Zijlema and Stelling (2003, 2005, 2008) developed a non-hydrostatic model (SWASH) with an edge based finite difference scheme for the approximation of the gradient in non-hydrostatic pressure at the interfaces between the vertical layers. Due to this calculation scheme, only two layers in the vertical direction are needed to get results with an accuracy and efficiency comparable with higher-order Boussinesq models (Stelling and Zijlema, 2003). The first results from this non-hydrostatic model for simulation of surf zone phenomena with the NLSW equations including non-hydrostatic pressure, seem very promising when compared to laboratory measurements, but the applicability of SWASH to the field is unknown.

## 2.5 Problem description and research focus

Wave propagation models are increasingly accurate for the dynamics in the nearshore zone, although discrepancies between computed and measured data still exist, especially at the location of abrupt changes in bottom topography and around the zone where waves break. The non-hydrostatic model of Zijlema et al. (2011) needs, in contradiction to Boussinesq models, no empirical relations for the initiation and energy dissipation by wave breaking. The performance of the model is good in comparison with laboratory measurements, but the accuracy of the cross shore wave dynamic predictions of this model has not been compared with field measurements yet.

Recent publications considering simulations with accurate wave models (Boussinesq and non-hydrostatic type models) are rarely paying attention to wave asymmetry and skewness. Although if a wave model should predict wave propagation and initiation of breaking in an accurate way, these parameters are as important as the prediction of wave height and the wave energy spectrum, on which most publications on wave model validation focus.

### Main research focus

To study the performance of the SWASH model for the evolution of wave height, wave energy-density, skewness and asymmetry across a natural intertidal sandbar.

### 3 Methodology

#### 3.1 SWASH model

The SWASH (Simulating Waves till Shore) model makes use of the nonlinear shallow water equations, including terms for non-hydrostatic pressure. This makes the model suitable for simulating wave transformation due to nonlinear wave-wave interactions, wave breaking and wave run-up. The equations in one-dimensional and depth-averaged form are as follows:

$$\frac{\partial \zeta}{\partial t} + \frac{\partial hu}{\partial x} = 0 \quad (12)$$

$$\frac{\partial u}{\partial t} + u \frac{\partial u}{\partial x} + g \frac{\partial \zeta}{\partial x} + \frac{1}{2} \frac{\partial q_b}{\partial x} + \frac{1}{2} \frac{q_b}{h} \frac{\partial(\zeta - d)}{\partial x} + c_f \frac{u|u|}{h} = \frac{1}{h} \frac{\partial}{\partial x} \left( h v_t \frac{\partial u}{\partial x} \right) \quad (13)$$

$$\frac{\partial w_s}{\partial t} = \frac{2q_b}{h} - \frac{\partial w_b}{\partial t} \quad (14)$$

$$w_b = -u \frac{\partial d}{\partial x} \quad (15)$$

$$\frac{\partial u}{\partial x} + \frac{w_s - w_b}{h} = 0 \quad (16)$$

Here,  $\zeta$  is the free surface elevation from still water level,  $d$  the still water depth,  $h$  the total water depth,  $u$  the depth averaged velocity in  $x$ -direction,  $w_b$  and  $w_s$  the velocity in  $z$ -direction at the bottom and the surface respectively,  $q_b$  the non-hydrostatic pressure at the bottom,  $c_f$  the bottom friction coefficient and  $v_t$  is the eddy viscosity. Further details and the numerical algorithms of the model are described by Zijlema et al. (2011).

Wave breaking is included in the model based upon the bore formation concept. This means breaking waves and bores are simulated as moving hydraulic jumps, automatically including energy dissipation. The pressure at the wave front of breaking waves should be hydrostatic, for this reason SWASH calculates the ratio between the vertical speed of the free surface and (a fraction of) the wave phase speed, as follows:

$$\frac{\partial \zeta}{\partial t} > \alpha \sqrt{gh}, \quad (17)$$

with  $g$  representing the gravitational acceleration. If the vertical speed of the free surface is higher than a fraction of the wave phase speed, non-hydrostatic pressure is neglected. The default value of  $\alpha$  is 0.6, corresponding with a maximum wave steepness of  $25^\circ$ . To represent the continuation of wave breaking, also if the wave front steepness is already below the critical value, non-hydrostatic pressure is also neglected when a neighboring grid point is flagged for hydrostatic computation and the local steepness is still high enough:

$$\frac{\partial \zeta}{\partial t} > \beta \sqrt{gh}. \quad (18)$$

In other words, waves start breaking when local steepness exceed  $\alpha$  and the pressure stays hydrostatic until the local steepness reaches  $\beta$ . The default value for  $\beta$  is 0.15.

Three different bottom friction values are available in the model: constant, Chezy and Manning. The option constant applies a dimensionless friction coefficient. With the Chezy and Manning options, the bottom friction coefficient is calculated as:

$$c_f = g/C^2. \quad (19)$$

In which  $C$  can be specified as a constant value when the Chezy option is used or is dependent on the Manning coefficient ( $n$ ) and the water depth ( $h$ ):

$$C = h^{1/6}/n. \quad (20)$$

Previous studies show surf zone dynamics to be better represented when the Manning coefficient is used (Zijlema et al., 2011).



## 3.2 Field campaign

### 3.2.1 Introduction to area

The data for this research were collected during a measurement campaign at the Dutch coast near Egmond aan Zee (beachpole 41.000) from October 27 until November 2, 2011. The studied area is the intertidal zone, which extends 100m from the high water line to a water depth of around 2m during high tide.

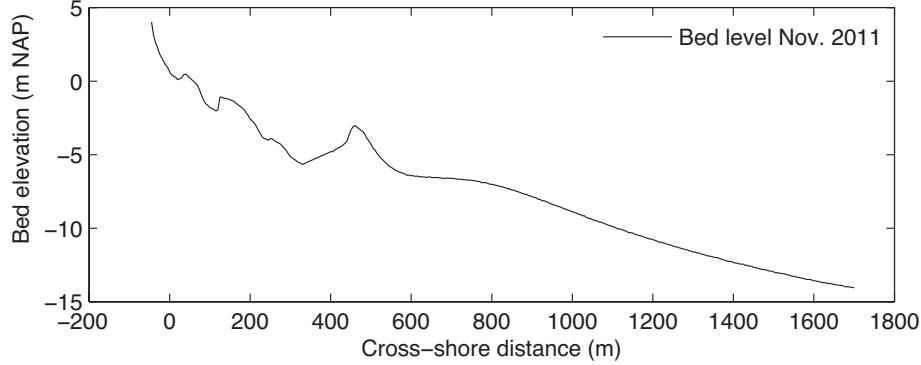


Figure 5: Bottom topography measured in the week following the measurement campaign, by Rijkswaterstaat. The intertidal zone is between  $x = -30$  and  $x = 80$ . NAP is local reference and equals about mean sea level.

The coastline at Egmond aan Zee is of constant concern due to erosion and the risk of flooding, in the past 300 years the village lost an area to the sea the same size as it is today. Since 1970, beach, and later also shoreface nourishments have been a measure to prevent further erosion of specific locations along the Dutch Coast. To protect the village Egmond aan Zee, substantial sand nourishments are implemented approximately every 5 years. At the exact location of the measurement campaign, three km south of the village, nourishments are not needed because the dune area is  $> 1\text{km}$  wide.

The morphology of the nearshore zone at this location consists of three sandbars (Figure 5). An outer subtidal bar, with a crest at a mean water depth of -2.5 to -4 m, an inner subtidal bar with the crest at a mean water depth of -1 to -3 m and an intertidal slip-face sandbar. The inner- and outer sandbar are migrating offshore during high-energy conditions and onshore during low-energy conditions (Ruessink et al., 2007). The intertidal sandbar is smaller in volume than the other two bars and can disappear completely during high-energy conditions. On the longrun ( $> \text{years}$ ) both subtidal bars move in offshore directed cycles (Wijnberg and Terwindt, 1995); the small bar at  $x=700\text{m}$  (Figure 5) is the remnant of a former outer bar.

### 3.2.2 Instrumentation

Measurement instruments were installed in a cross-shore transect in the intertidal zone across an intertidal sandbar (Figures 6, 7 and 8). This transect consisted of nine pressure gauges (OSSI, Ocean Sensor Systems Inc.) and three mini-frames, equipped with a pressure sensor, an electromagnetic flowmeter (EMF), measuring cross-shore and longshore current velocities, and three optical backscatter sensors (OBS), measuring sediment concentrations on different heights above the bed. Additionally one tripod was equipped with a pressure sensor, an acoustic doppler velocimeter (ADV) and one OBS. The instruments on the three mini-frames collected data with a frequency of 4Hz, all other instruments with 5Hz. The mini-frames and tripod also contained a float, initiating the measurements when submerged and stopping measurements when emerged from the water. The data from the mini-frames was retrieved every day during low tide, the data from the separate pressure gauges and the ADV tripod were retrieved twice during the measurement campaign.

The height of all instruments above the bed was measured every day and adjusted when needed. The pressure gauges were kept at a height of 0-20 cm above the bed, depending on the location, with lower heights in the swash zone to record run-up of waves on the beach. The height of the ADV sensor was kept between 20 and 40 cm above the bed, and was measuring current velocities 18cm below the sensor. Although the height of the instruments were measured and adjusted every day, it was not possible to prevent them from exceeding those ranges with a maximum of 15 cm, especially during high-energetic conditions. The instrument heights between the measurements were linearly interpolated.

The bottom topography of the intertidal zone along the transect was measured with DGPS every day, except for days with strong wind. The profiles were linearly interpolated to obtain beach profiles during high tide. The DGPS device was also placed on a quad every other day to create a digital elevation model of the study area, with a coverage from 500 meter south to 500 meter north of the cross-shore transect.

Besides the pressure gauges, deep water wave spectra with a temporal resolution of 30min are also available. These were measured approximately 15 km southwards of the transect, in 26m water depth, in front of the the city IJmuiden.

The intertidal and nearshore zones were monitored using time-exposure video images with an interval of 30 minutes and for part (from October 3-23) of the measurement campaign with 2 Hz during daylight. The time-exposure images are useful to determine the location of wave breaking (Price and Ruessink, 2008), as a support to the location calculated with the cross-shore change in energy flux along the measurement transect. The 2Hz images can be used to extract a runup timeseries, which makes it possible to extend this study to the swash zone in the future. This was, however, not performed in the framework of the present study.

### 3.2.3 Hydro- and morphodynamics

A large variety in weather conditions during the measurement campaign resulted in an interesting dataset (Figure 9). Low-energetic conditions were interrupted by two high-energetic periods, with significant wave heights up to 3.8m in 26m water and 1.5m in the intertidal zone. The wave energy period ( $T_{m-10}$ ) ranged from 4-6s during low and intermediate energetic conditions and 6-8s during high-energetic conditions. The offshore wave angle of incidence was varying



Figure 6: Overview of the cross-shore transect in seaward direction during low tide (left) and view at the instruments in shoreward direction in the last week of the field campaign, with in front a pressure gauge, followed by the tripod with ADV and one of the three mini-frames (right).

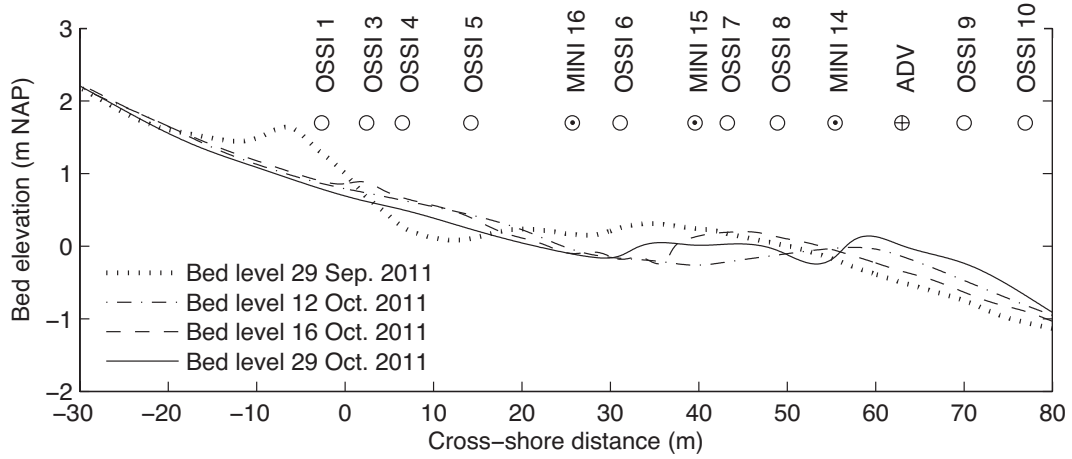


Figure 7: Dynamics of the bottom profile in the intertidal zone near Egmond aan Zee, measured during the field campaign in 2011. The locations of the instruments and their names are also indicated with pressure sensors (o), miniframes (⊙) and the ADV frame (⊕).

throughout the field campaign, but the angle of incidence in the intertidal zone was, due to refraction, always within  $20^\circ$  from shore normal. Tidal water level variations were around 2m, with a maximum set-up (difference between astronomical predicted and measured water level) of 0.85m during the storm around day 10.

As a result of the heterogeneity in wave conditions during the field campaign, the bottom topography changed considerably (Figures 7 and 8). The campaign started with a beach with a steep berm and high intertidal sandbar; this profile flattened during the first storm (bed level of Oct. 12 in Figure 7). In the weeks following the first storm the intertidal bar repeatedly grew and reduced depending on the hydrodynamic conditions. During the last week, with low-energetic conditions, the bar migrated in the seaward direction and split in two parts with a trough in between (bed level of Oct. 29 in Figure 7). This is also illustrated by the images taken by the Argus tower during low-tide (Figure 8).

### 3.2.4 Data analysis

Measured pressure signals were corrected for air pressure as measured by a local device, and converted into water elevation above the sensor. Thereafter, the elevation was converted with linear wave theory to sea surface time series. Water depths ( $h$ ) were calculated as the mean of the measured elevation plus the instrument height.

Wave energy spectra  $E(f)$ , where  $f$  is frequency, were calculated for time-series with a length of 28 minutes, dividing them in 512s long, Hanning window blocks and 50% overlap. This resulted in a 95% confidence range of 0.75-1.41 (78 degrees of freedom). Wave heights were calculated as

$$H_{m0} = 4\sqrt{m_0}, \quad (21)$$

with  $m_0$  as the zeroth moment of the energy spectra. The high frequency (HF) and low frequency (LF) wave height were taken as the zeroth moment of only part of the spectrum, with HF  $0.05 < f < 1\text{Hz}$  and LF  $f < 0.05\text{Hz}$ . The HF skewness and asymmetry of the wave signal were calculated using Equations 1 and 2, respectively.

The bispectra were calculated with the timeseries divided in blocks of 512s long, with frequency band averaging set to three bands. This results in 186 dof and a 95% significance level for non-zero bicoherence of 0.18.

The wave angle of incidence was taken as the energy-weighted mean angle, calculated as the orientation of the dominant axes in a covariance matrix between measured HF  $u$  and  $v$  at the ADV, with  $u$  and  $v$  as the instantaneous cross-shore and alongshore velocity respectively.

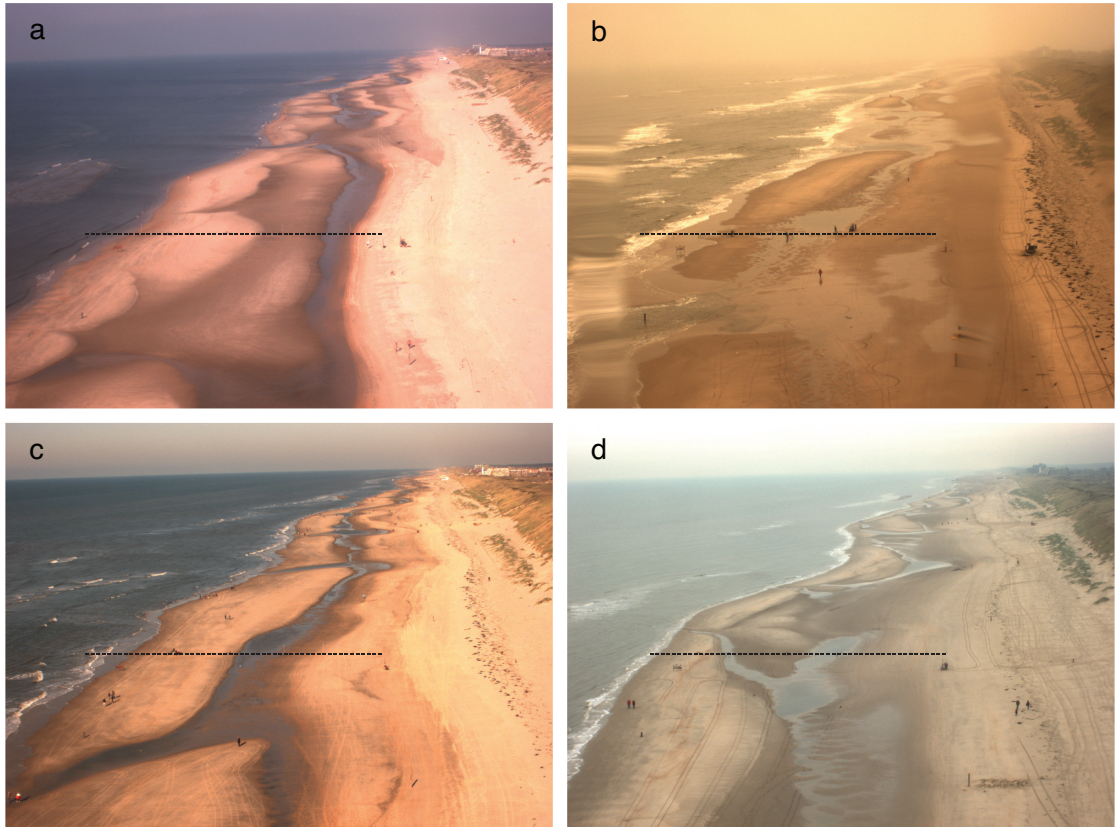


Figure 8: Morphodynamics in the intertidal zone during the field campaign near Egmond aan Zee. The pictures are taken on (a) September 29, (b) October 12, (c) October 16 and (d) October 29, 2011. Measured bottom profiles at these dates are plotted in Figure 7. The dashed lines indicate the location of the transect with instruments.



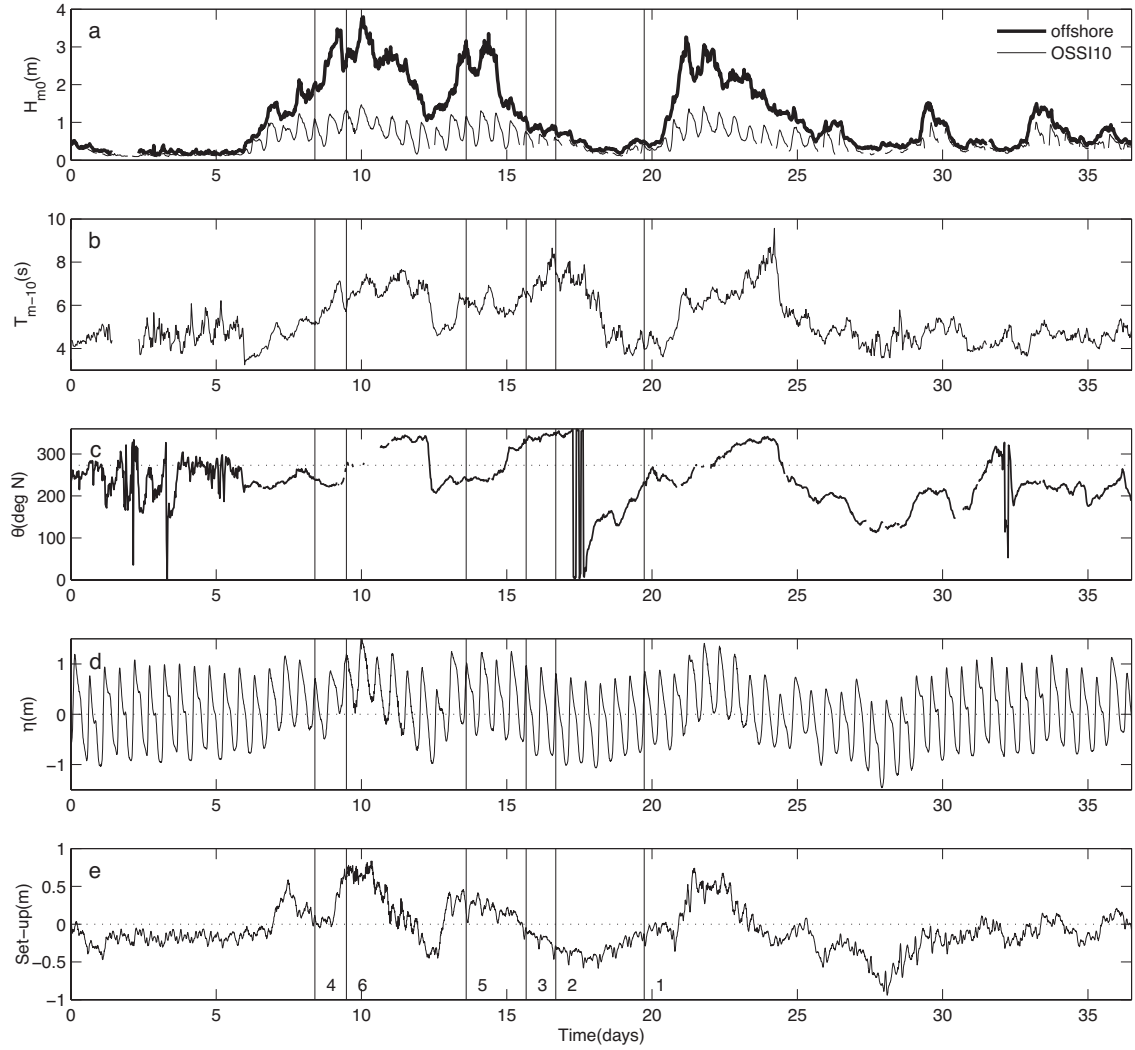


Figure 9: Offshore (at station 'stroommeetpaal') wave conditions and water levels during the field campaign. From top to bottom, the wave height measured offshore and at the most seaward pressure gauge in our transect (a), wave period (b), offshore wave angle of incidence with a reference line for shore normal (c), measured water levels (d) and measured set-up (e) calculated by subtracting tidal predictions from measured water levels. The time axis is in days from the first day of the field campaign. The selected cases are indicated by the vertical lines in the time series.



The breaking zone was determined from the time-exposure video images by the difference in pixel intensity between regions with breaking and non-breaking waves. Regions with breaking waves showed a higher pixel intensity, caused by the foam on breaking waves (see Figure 10). This gives a relative value for wave breaking for each cross-shore location per case, but cannot be used to compare the cases with each other, as the light conditions differ (amount of sunshine and sun angle).

### 3.3 Data selection

For the analysis and simulations, six representative cases were selected from the collected data set. The selection procedure was based upon stationarity, data availability and high frequency wave height at OSSI 10. Furthermore the wave angle of incidence and amount of reflection of the selected cases are discussed to be able to explain a possible mismatch between observations and predictions in the results section.

First the time periods around high tide were selected, those 71 periods are more useful for two major reasons. It increases the data availability, as higher water reaches further inland and thereby more instruments were submerged. The second reason is stationarity, which is reasonable to find during slack-water high tide in comparison to periods with raising or falling water levels. Another advantage of high water levels is the higher probability to capture all different coastal regimes with the array, from the shoaling to the swash zone. Data availability does not only depends on the water level, also some instruments were not functioning properly all the time due to natural causes (storm damage or covered by sand) and non-natural causes (technical issues). Only the high tide periods with data available from at least 11 pressure instruments were picked for further analysis. Furthermore, only cases were selected from periods with 2Hz video images available, to make it easier to extend this research to the swash zone in the future.

Eventually six cases, representing the whole range of energetic conditions during the campaign, were chosen that met the above requirements (Figures 9 and 10). The cases are numbered from 1-6, in order of measured high frequency wave height ( $H_{m0}$ ) at OSSI 10 (Table 3). The bottom profiles of these cases (Figure 11) show the whole variety encountered during the measurement campaign, as shown in Figure 7.

Table 1: Wave statistics of the six selected cases at the stroommeetpaal (stm) and at OSSI 10 (OS 10), the cases are numbered in the order of increasing wave height (measured at OSSI 10).

Cases	Date/Starttime (MET)	$H_{m10}$ stm [m]	$T_{m10}$ stm [s]	$H_{m0}$ OS 10 [m]
1	16-Oct 17:30	0.5	4.0	0.40
2	13-Oct 16:30	0.9	7.4	0.55
3	12-Oct 16:00	1.1	6.4	0.71
4	4-Oct 8:30	2.0	5.1	0.84
5	20-Oct 8:30	3.2	6.4	0.91
6	6-Oct 11:30	2.7	5.8	1.32

The cases are used as input and validation data for the model in one-dimensional mode, in which the wave angle of incidence is not taken into account. The wave angle of the six selected cases are all within 20 degrees from normal incidence at the location of the ADV frame. The influence of these small angles on the wave height was calculated with the Battjes Jansen model (Battjes and Janssen, 1978), of which the free parameter  $\gamma$  is calculated as described by Ruessink et al. (2003). All cases were simulated with a measured wave angle at the location of the ADV frame and with a wave angle of normal incidence. The resulted wave height evolution for both angles barely differed, with an increase towards the shore and with wave height. The maximum difference in wave height between the two wave angles is 0.001m for the case with the lowest



Figure 10: Time averaged images of Egmond aan Zee during the six cases. The location of the cross-shore measurement transect is especially visible during low-energetic conditions, just below the middle of the images. The images also show the date, time and high frequency wave height ( $H_{m0}$ ) at OSSI 10. The cases are ordered by increasing wave height.

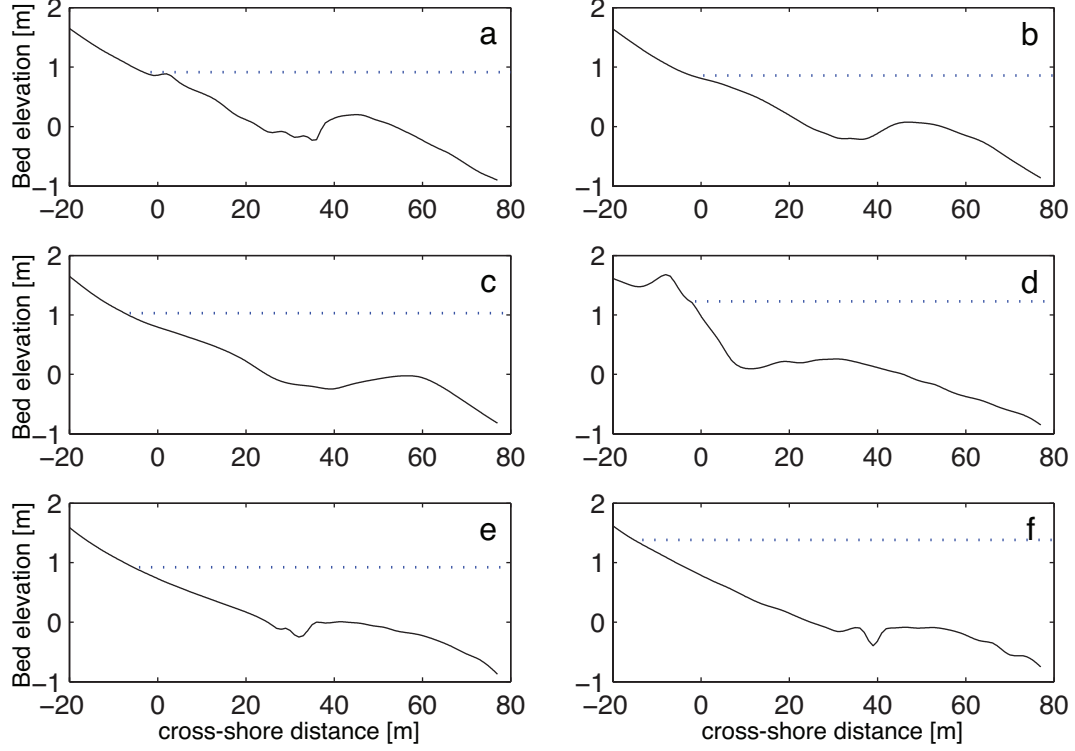


Figure 11: Bottom profiles for the selected cases (a) 1 - (f) 6. The dotted lines represent the still water level.

waves and  $0.02m$  for the highest waves. These differences are considered negligible and the cases can thus be used for the validation of the one-dimensional model.

The water surface time series at the seaward boundary of the wave model has to consist of only the shoreward propagating waves, whereas the pressure sensors measured shoreward and reflected seaward propagating waves together. To calculate the amount of reflection in each time series, the velocity measurements of the ADV sensor are used to decompose the water level measurements in a shoreward and a seaward propagating component as (Guza et al., 1984),

$$PC(t) = (\eta + \left(\frac{h}{g}\right)^{1/2} u)/2, \quad (22)$$

$$MC(t) = (\eta - \left(\frac{h}{g}\right)^{1/2} u)/2. \quad (23)$$

$PC(t)$  and  $MC(t)$  are the shoreward and seaward propagating components respectively. The reflection coefficient for each frequency is calculated by dividing the wave energy density spectra of  $MC(t)$  over  $PC(t)$ , resulting in a coefficient from 0 (no reflection) to 1 (all incoming energy is reflected).

The reflection coefficient per frequency ( $0-0.1Hz$ ) is visualized in Figure 12. It is important to note that near zero energy density of both  $MC(t)$  and  $PC(t)$  also results in a high reflection coefficient. Reflected wave energy decreases in general with increasing frequency. high-energetic cases 5 and 6 show a high reflection coefficient for the low frequencies (infragravity waves). For all cases except case 4, reflection is minimal for frequencies  $> 0.05Hz$ . Case 4 shows reflection for a broader range of frequencies, this can be directly linked with the steep beach face (Figure 11d).

Decomposition of water surface time series in an incoming and outgoing component is only possible when also current velocities are available on the same location. Hence decomposition of water surface data for the seaward boundary is possible at the location of the ADV, but unfortunately this is not possible for OSSI 10. In an attempt to include the  $\approx 15m$  seaward of

the ADV, the sensitivity of the model predictions to different timeseries at the seaward boundary is discussed in Section 3.5.3.

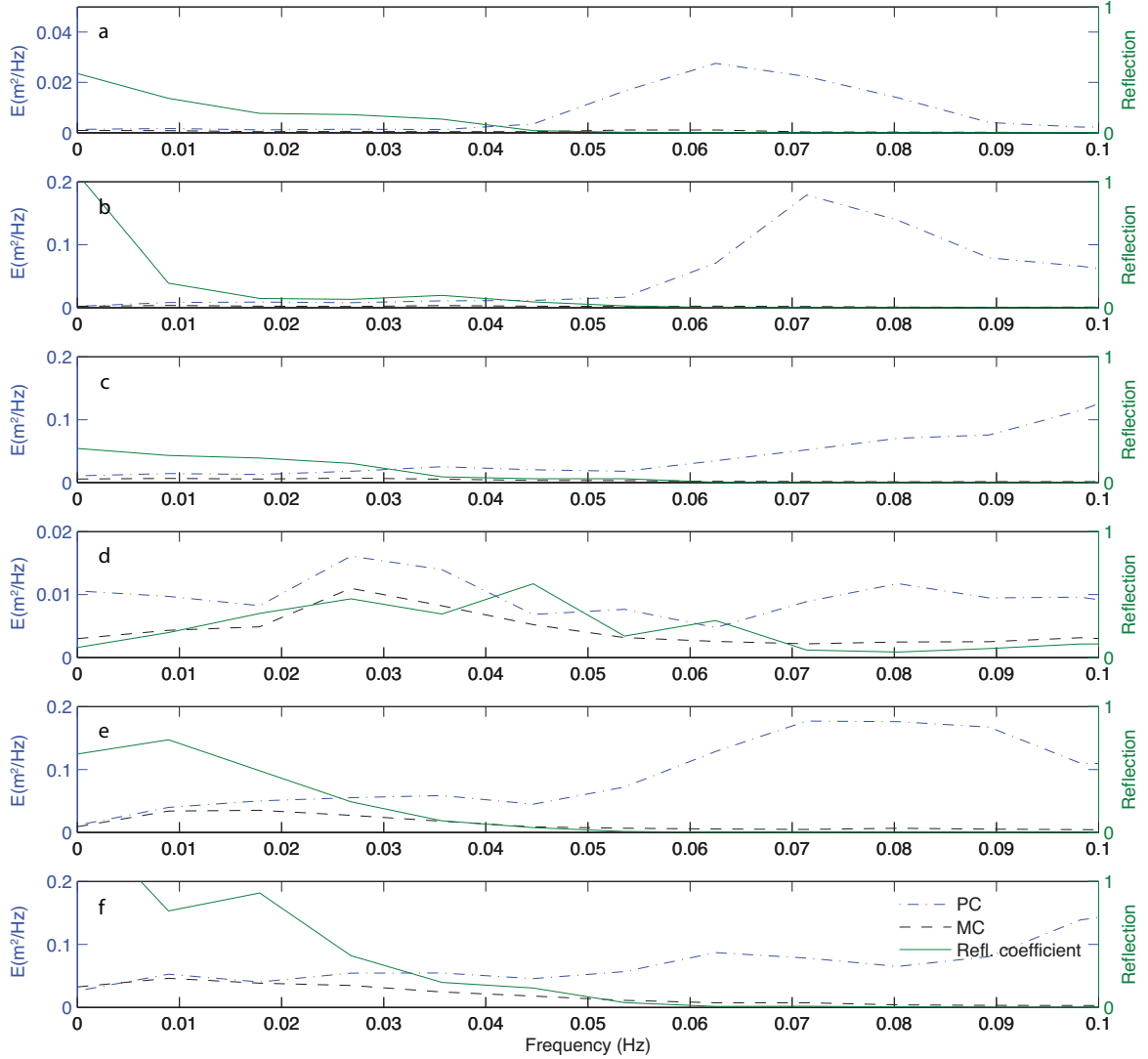


Figure 12: Energy density spectrum (0 - 0.1Hz) for the cases (a) 1 - (f) 6, decomposed in a shoreward (---) and seaward (- -) propagating component, the ratio results in a reflection coefficient (—).

### 3.4 Model implementation

The discretization and calculation scheme were set to the default for SWASH version 1.10AB. The initial timestep was set to 0.02s, the minimum and maximum courant number to 0.1 and 0.5 respectively and one vertical layer was used. Increasing the amount of vertical layers is especially important to account for wave dispersion, but as all the simulations were performed in shallow waters (< 2 m depth), dispersion is small. The model was run for a duration of 28 minutes, of which the last 25 minutes were used for the analyses to eliminate the time needed for initialization. The spatial resolution and friction value was determined after a sensitivity analysis in the next section.

The model needs two types of input data for the performed simulations, a bottom profile and a forcing at the seaward boundary. The bottom profile was generated from the DGPS measurements, interpolated to get the bottom profile at the starttime of each case. The water level at the seaward boundary was forced using (filtered) measured time-series at OSSI 10 or ADV.

The output of the model simulations were the waterlevel, waterdepth and presence of breaking, as sections with a cross-shore resolution of 1 m and a temporal resolution of 0.2s. The presence of breaking indicate where hydrostatic pressure is assumed by the breaking formulation (Equations 17 and 18), with a value of 0 (no breaking) or 1 (breaking). The breaking output was averaged over time, which gives per location a percentage of time for which faces of breaking waves or bores are passing. This compares well with the time-exposure video images taken during the campaign, as the face of breaking waves and bores are producing foam and as a consequence lighter pixels in the images (see also Section 3.2.4). Other wave statistics are calculated from the model output as described in Section 3.2.4.

### 3.5 Sensitivity analysis

To find the appropriate settings in SWASH for the simulation of wave propagation in the intertidal zone; sensitivity analysis were performed by changing the spatial resolution of the computational grid and the friction coefficient.

#### 3.5.1 Spatial resolution

To investigate the influence of the spatial resolution of the computation grid on the model results, simulations were performed in the intertidal zone with a grid resolution of  $0.2m$ ,  $0.1m$ ,  $0.05m$ ,  $0.02m$  and  $0.01m$ . For these simulations the measurements of case 3 and 5 were used. The seaward boundary is represented by the time series measured with OSSI10. The bottom friction coefficient was kept constant along the transect, with a value of 0.003.

The differences between the predicted data within the resolution range is comparable for cases 3 and 5 (Figure 13). The sensitivity of the HF wave height is minimal, with a slight increase in the zone landward of the trough. The LF wave height shows a higher sensitivity to mesh size, particular landward of the sandbar crest, which is located at  $x \approx 60$  and  $x \approx 40m$  for case 3 and 5 respectively. The skewness of the HF signal is slightly changing for different grid resolutions, and becomes unstable for the finest mesh size ( $0.01m$ ) in combination with the conditions of case 5. The most sensitive to grid resolution is the asymmetry of the HF wave signal, it changes throughout the whole cross shore section. In general the asymmetry increases (becomes more negative) for finer resolutions.

To conclude, an increase in spatial resolution below  $0.2m$  is not necessary for predictions of the HF and LF wave heights, but the skewness and in particular the asymmetry change significantly for a finer resolution. Convergence of the wave shape predictions was not reached within the used resolution range, but computation time and arising instability limited further simulations with an even finer resolution. For these reasons, a mesh size of  $0.02m$  was chosen for further simulations and analysis. This resolution is a compromise between accuracy and computation time, as a mesh size of  $0.01m$  increases the calculation time from 1.5 to 8 hours per case.

#### 3.5.2 Bottom friction

The only optimized coefficient for the simulations is the bottom friction, in the form of the manning roughness coefficient. The manning roughness is for natural beaches typically between 0.02 and 0.03. The difference in wave shape evolution between Figure 13 (constant friction) and Appendix A (depth dependent friction) show a depth-dependent friction formulation is performing better in wave shape predictions.

The high-frequency  $H_{m0}$  showed a very low sensitivity to bottom friction, in the order of a 0.01 difference in rms error between  $n = 0.02 - 0.03m^{1/3}/s$ . The lowest rms error for  $H_{m0}$  was found for  $n = 0.026m^{1/3}/s$  for all cases. Including the rms-error in predicted low-frequency  $H_{m0}$  was not useful for friction optimization, as those values are over-predicted for other reasons and



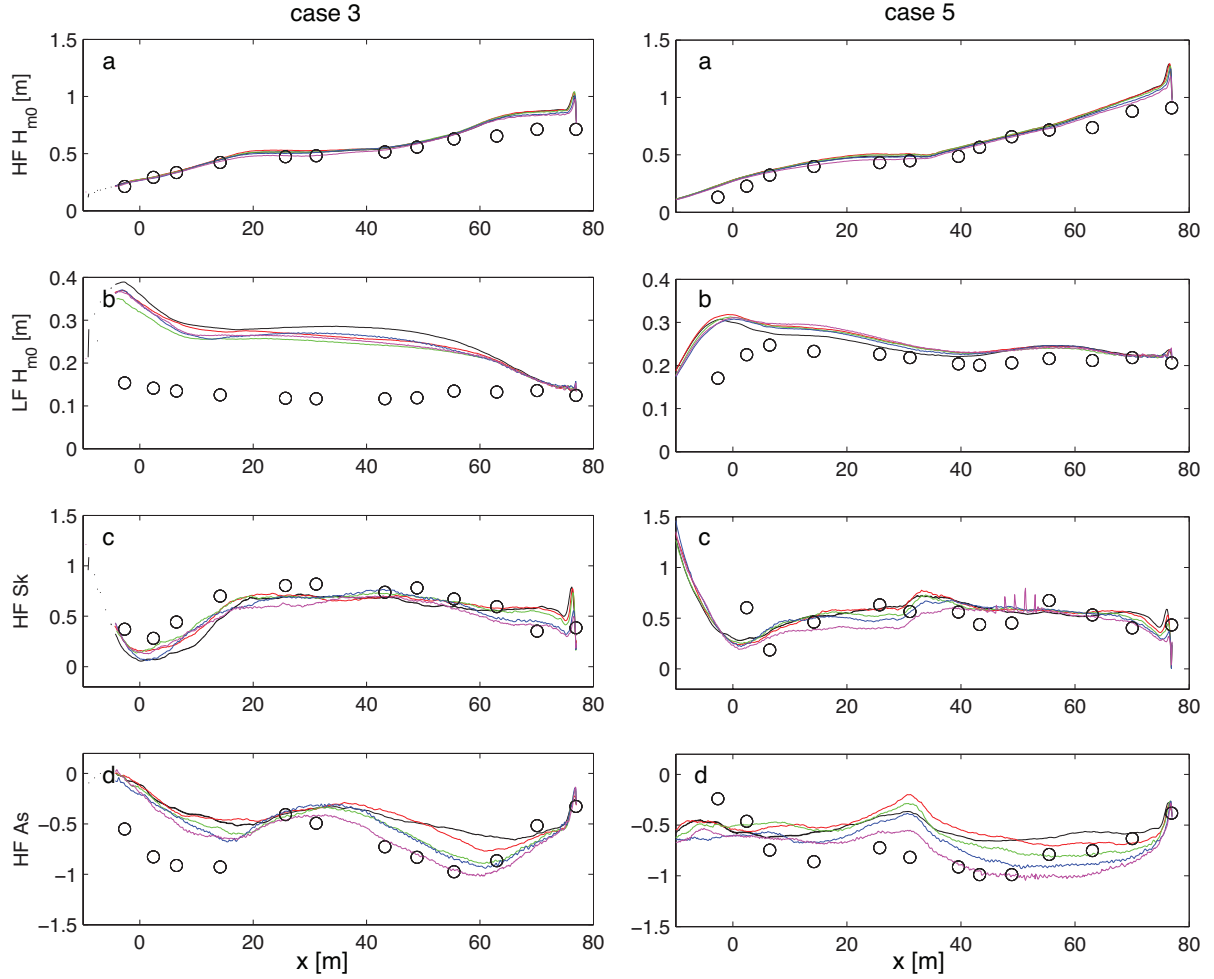


Figure 13: Sensitivity of predicted (a) high frequency  $H_{m0}$ , (b) low frequency  $LFH_{m0}$ , (c) skewness and (d) asymmetry of case (left) 3 and (right) 5 for mesh size. Mesh sizes (black) 0.2m, (red) 0.1m, (green) 0.05m, (blue) 0.02m and (magenta) 0.01m.

very high friction values are needed to compensate those. The value  $n = 0.026m^{1/3}/s$  is more often used to represent the bottom friction at the beach of Egmond aan Zee, i.e. van Duin et al. (2004), further supporting the correctness of this value.

### 3.5.3 Offshore boundary forcing

The boundary at the offshore side of the model was for all simulations forced with measured time series. The time series measured at the ADV frame, filtered for only incoming waves, and OSSI 10, unfiltered and high frequency ( $f > 0.05\text{Hz}$ ) filtered, were tested for all cases to discover the differences. Forcing with only the incoming waves is supposed to be the closest to reality, but it is worthwhile to also look at forcing with measurements further seaward. To discover the influence of filtering for high frequency waves, and thereby taking out most of the reflected waves (Figure 12), simulations were done with high frequency filtered time series measured at OSSI 10 as wave forcing.

The cross shore statistics for the three simulations per case were added as Appendix A. To select the most appropriate boundary forcing and to get more insight in the contribution of different parts of the wave signal at the boundary, predictions were compared with observations. The difference between these were quantified with the root mean square (rms) error, calculated per case and for each location.

In this section only the differences between the three types of boundary conditions are

discussed, other patterns in the predictions are dealt with in the results section. The simulations with only hydrostatic pressure, which are plotted in the same figures, are discussed in the next section.

The predicted HF wave heights show a relatively low error per case (Figure 14a). The simulations with only incoming waves at the location of the ADV seem to represent the observed wave heights best. This is mainly caused by the section  $x > 50\text{m}$  (Figure 15a), but these predictions also show slightly lower errors in the shallower part of the section.

The main difference between the used time series at the seaward boundary is found in the LF part of the wave signal, though the resulting rms error values per case are comparable (Figure 14b). Filtering for only incoming waves does not make a significant difference.

The variability of the error value for skewness depends more on location and case, then on the type of forcing at the boundary. This dependence is also visible for the asymmetry (Figures 14d and 15d).

To conclude, filtering the time series used at the seaward boundary for high frequencies did not result in better predictions, but filtering for incoming waves did result in lower errors for the high frequency energy. The error for  $Sk$ , with only incoming waves at the boundary, is slightly lower throughout the profile but  $As$  shows slightly higher errors. Because of the importance of accurate predictions of the high-frequency  $H_{m0}$ , it is chosen to continue with the simulations with only incoming waves at the seaward boundary. This means the two most seaward pressure sensors are not used for model validation, but high errors in the predictions, due to boundary effects, already made these locations not suitable for validation.

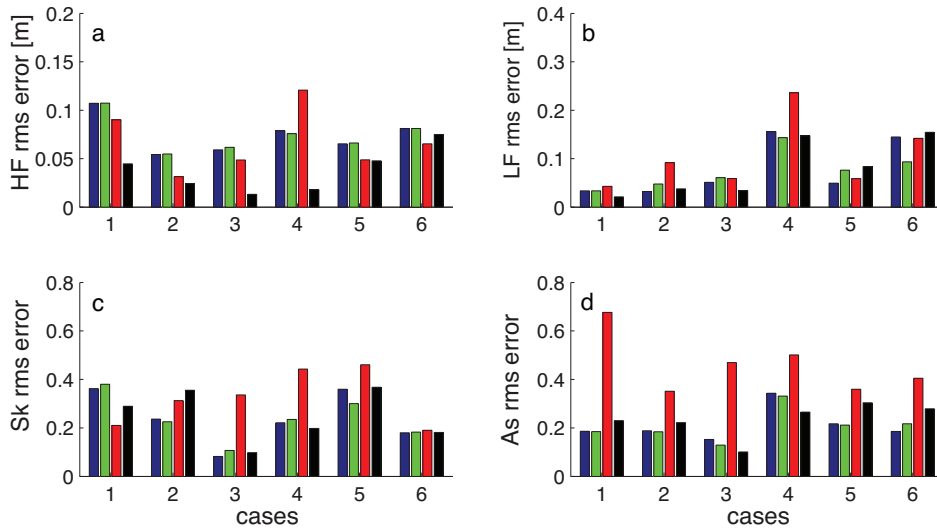


Figure 14: Root mean square (rms) error for (a) HF  $H_{m0}$ , (b) LF  $H_{m0}$ , (c) HF  $Sk$  and (d) HF  $As$  per case for three different offshore boundary conditions. The colors of the bars indicate the type of forcing, (blue) unfiltered time series measured at OSSI 10, (green) HF filtered time series measured at OSSI 10, (red) unfiltered OSSI 10 but only hydrostatic computation and (black) time series measured at ADV filtered for only incoming waves.

### 3.5.4 Hydrostatic and non-hydrostatic pressure

The high frequency wave height and shape show boundary effects at the seaward boundary for the different types of forcing described in the previous section (see Appendix A for an overview of predictions). These boundary effects are due to the use of water height time series as boundary forcing, which consists only of instantane hydrostatic pressure. The lack of the non-hydrostatic part of the pressure at the boundary means some distance is needed to overcome this. These boundary effects explain the high rms error for the high frequency wave height at  $x \approx 50 - 80\text{m}$  (Figure 15).

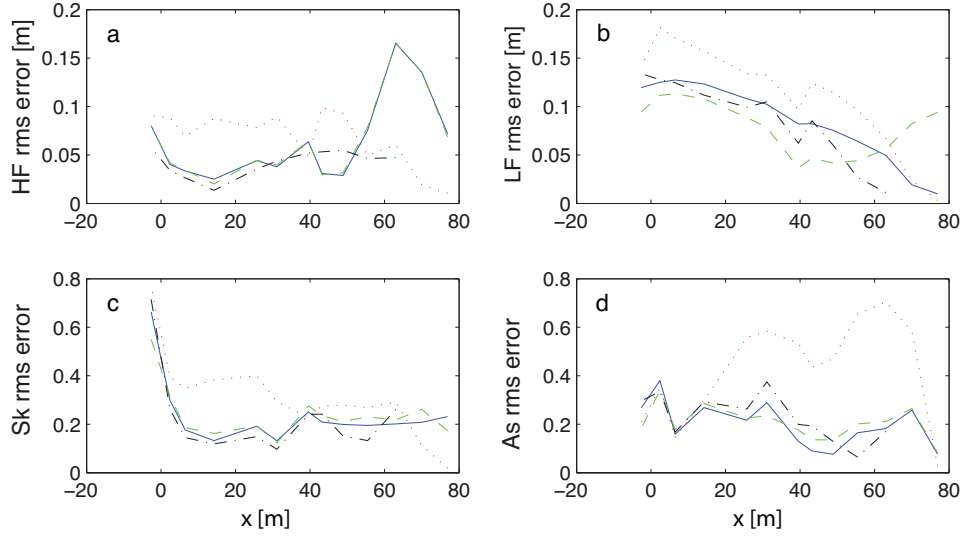


Figure 15: Root mean square (rms) error for (a) HF  $H_{m0}$ , (b) LF  $H_{m0}$ , (c) HF  $Sk$  and (d) HF  $As$  per instrument location for three different offshore boundary conditions. The lines show, (solid & blue) unfiltered time series measured at OSSI 10, (dashed & green) HF filtered time series measured at OSSI 10, (dotted & red) unfiltered time series measured at OSSI 10 but only hydrostatic computation and (dot-dashed & black) time series measured at ADV filtered for only incoming waves.

To test this hypothesis, the six cases were also simulated with only hydrostatic pressure. The wave height and shape predictions are shown in Appendix A and their corresponding errors in Figures 14 and 15. The boundary effects are not present anymore for those simulations, confirming the idea these are caused by an absence of non-hydrostatic pressure at the seaward boundary in case non-hydrostatic pressure is included in the computations.

Eliminating non-hydrostatic pressure from the simulations reduces the governing equations to the nonlinear shallow water (NLSW) equations. These equations are valid for broken waves and wave run-up, but are not applicable in the pre-breaking region. These equations predict the front face of a wave or bore to steepen until it is vertical, the non-hydrostatic pressure compensates for this steepening. This compensation is clearly missing in the hydrostatic simulations, as shown by an over-prediction of wave asymmetry for all cases (Appendix A). The discrepancy in HF wave height between the simulations with and without non-hydrostatic pressure versus observations is smaller for high-energetic conditions (Figure 14a), as more waves are broken within the model domain and the NLSW equations without non-hydrostatic pressure are actually valid. The over steepening of the waves for lower energetic cases is also reflected in more dissipation in the high frequencies and as a result an under-prediction of the short wave heights (see Appendix A). For these reasons, non-hydrostatic pressure is included for the validation of the SWASH model.

## 4 Results

The discussion of the results for the six cases starts in Section 4.1 with the location of wave breaking, this is an important factor, as it is directly related with wave shape and energy dissipation. A comparison between observations and predictions of the high-frequency wave height ( $H_{m0}$ ) is presented in Section 4.2, before the wave energy is discussed in more detail in Section 4.3. The main focus of our validation, the evolution of the wave shape across an intertidal sandbar, is discussed in Section 4.4.

### 4.1 Breaking

The observed breaking (Figures 16-21 for case 1-6) was extracted from the time-exposure images as the pixel intensity along the measurement transect. These graphs show two main peaks for all cases, one for breaking above the intertidal sandbar and more shoreward smaller waves break above the beach face and in the swash zone.

The first peak of observed wave breaking is located around the top of the intertidal sandbar and shows a seaward shift with increase in  $H_{m0}$ . These breaking peaks become also wider with an increase in wave energy, as bores are present throughout the transect. Cases 5 and 6 are both located in the surf zone, as waves already break seaward of the instrument transect (visible in Figure 10). Case 4 shows a short and high breaking peak above the beach face, corresponding with the high slope steepness.

The predicted wave breaking, as percentage of time where pressure is taken hydrostatic due to the presence of a breaking wave face or bore, is shown in Figures 16d-21d. These breaking predictions show for the high-energetic cases also boundary effects at the seaward side. The predictions do reproduce the observed trend in cross-shore presence of breaking waves and bores and the peak above the sandbar crest is predicted on the right location.

The predictions show a sharp peak close to the wet-dry boundary of the model, which is not seen in the light intensity observations. This is probably caused by the presence of small bores in this zone, which do not have enough foam to cause a higher light intensity in the time-exposure images.

### 4.2 High frequency wave height

As the locations of short wave breaking are well predicted by the model, we focus next on the cross-shore development of the high-frequency wave height ( $H_{m0}$ ). At the seaward side of the field transect ( $x=76.9\text{m}$ ),  $H_{m0}$  varies between 0.4 and 1.32m for case 1 to 6 respectively, and decreases in shoreward direction (Figure 22). For the low-energetic cases (1-3), the wave height remains stable until the top of the intertidal sandbar, where waves dissipate part of their energy due to breaking. Only case 1, the least energetic case, shows some wave shoaling slightly seaward of the top of the sandbar, around  $x=50\text{m}$ . Above the trough, the wave height stabilizes, followed by another dissipative zone at the beach face. The high-energetic cases 5 and 6 show dissipation throughout the profile, but less above the trough. These locations of wave energy dissipation agree with the earlier discussed locations of wave breaking.

Table 2: Predicted versus observed high-frequency wave height rms error per case.

Cases	1	2	3	4	5	6
rms error	0.04	0.02	0.01	0.02	0.05	0.08

The wave height evolution of case 4 is quite distinct from the other cases, which finds its origin in the beach profile. The sandbar is with a seaward slope of 0.03 less profound and the

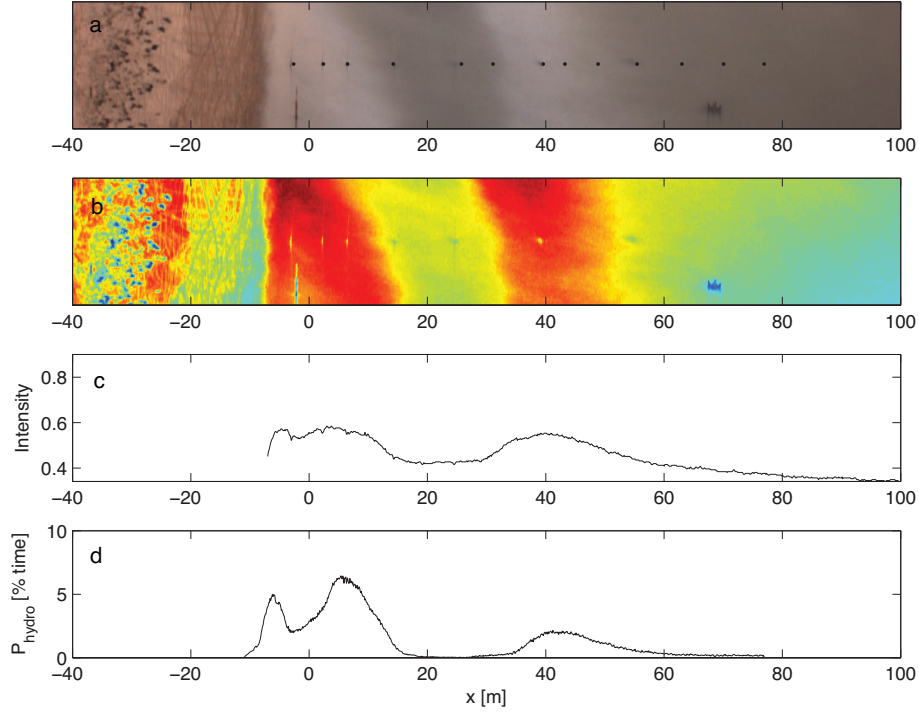


Figure 16: Case 1 - Observed and predicted wave breaking along the cross-shore transect. The extraction of wave breaking from the time-exposure images is shown as, (a) the original time-exposure image with (black dots) the location of the pressure sensors, (b) the pixel intensities in the image and (c) pixel intensity along the cross-shore measurement transect. The (d) predicted breaking is shown as the percentage of time where pressure was taken hydrostatic because of the presence of a breaking wave or bore.

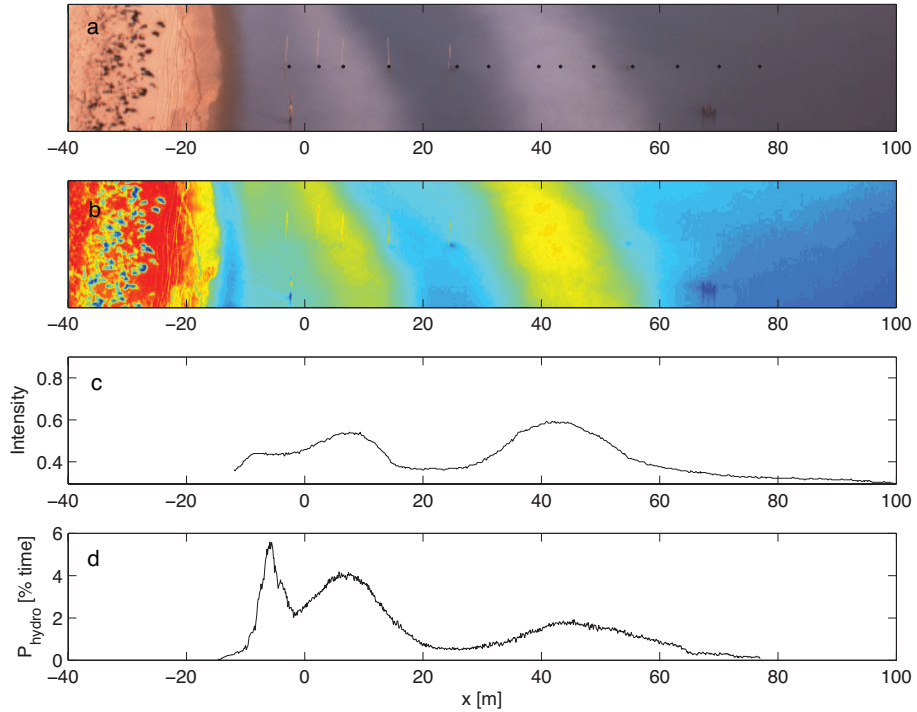


Figure 17: Case 2 - Observed and predicted wave breaking along the cross-shore transect. The extraction of wave breaking from the time-exposure images is shown as, (a) the original time-exposure image with (black dots) the location of the pressure sensors, (b) the pixel intensities in the image and (c) pixel intensity along the cross-shore measurement transect. The (d) predicted breaking is shown as the percentage of time where pressure was taken hydrostatic because of the presence of a breaking wave or bore.

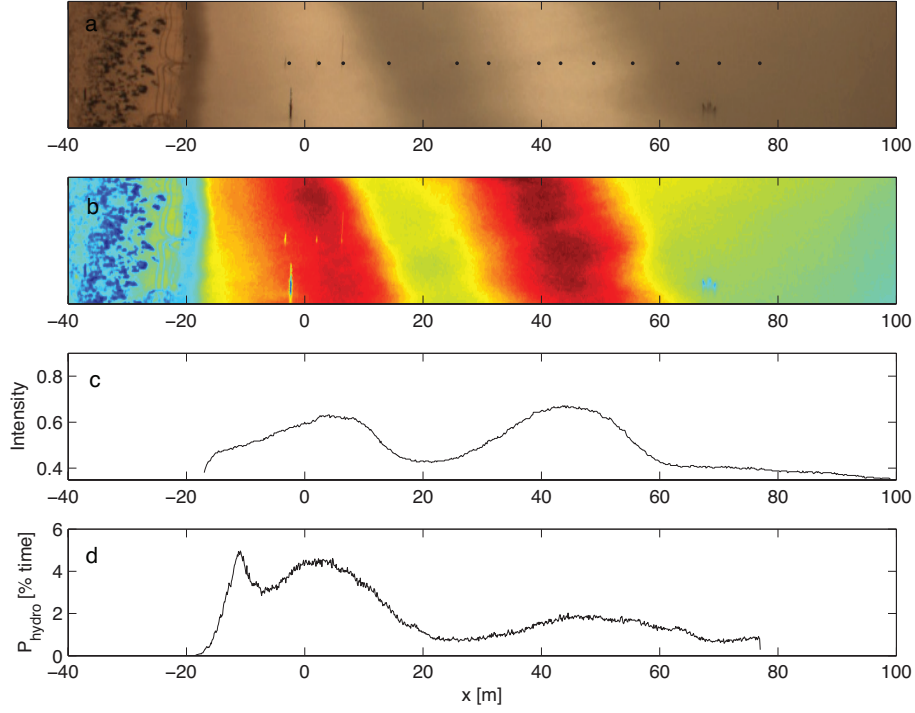


Figure 18: Case 3 - Observed and predicted wave breaking along the cross-shore transect. The extraction of wave breaking from the time-exposure images is shown as, (a) the original time-exposure image with (black dots) the location of the pressure sensors, (b) the pixel intensities in the image and (c) pixel intensity along the cross-shore measurement transect. The (d) predicted breaking is shown as the percentage of time where pressure was taken hydrostatic because of the presence of a breaking wave or bore.

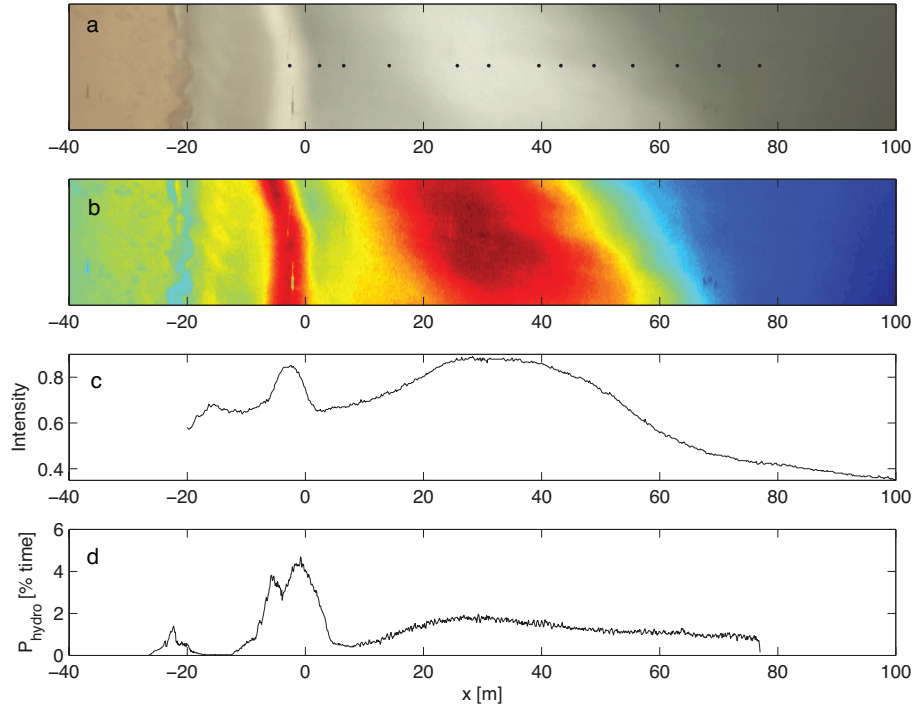


Figure 19: Case 4 - Observed and predicted wave breaking along the cross-shore transect. The extraction of wave breaking from the time-exposure images is shown as, (a) the original time-exposure image with (black dots) the location of the pressure sensors, (b) the pixel intensities in the image and (c) pixel intensity along the cross-shore measurement transect. The (d) predicted breaking is shown as the percentage of time where pressure was taken hydrostatic because of the presence of a breaking wave or bore.

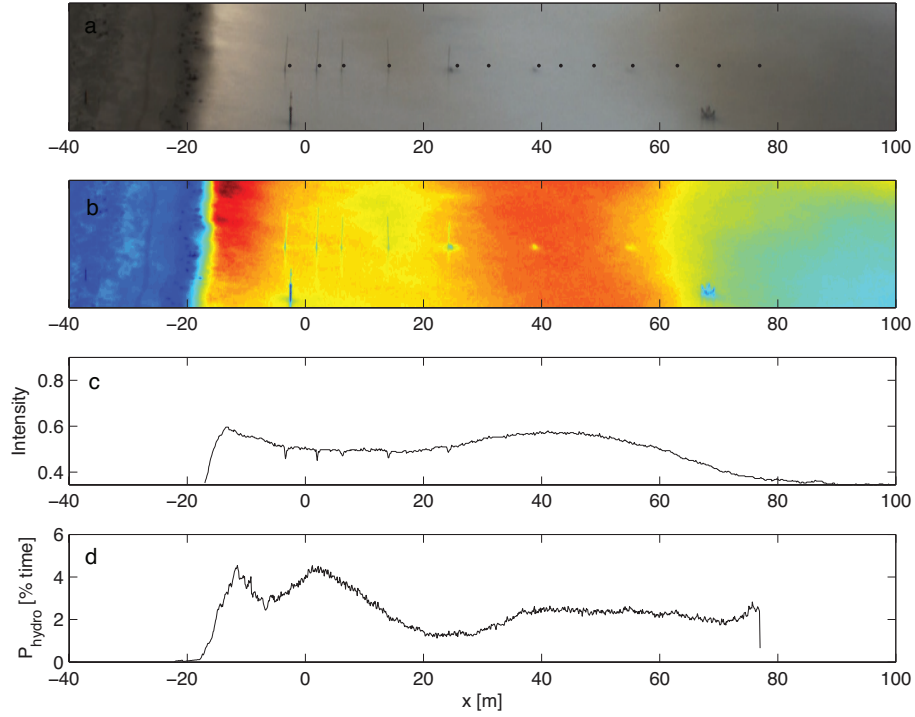


Figure 20: Case 5 - Observed and predicted wave breaking along the cross-shore transect. The extraction of wave breaking from the time-exposure images is shown as, (a) the original time-exposure image with (black dots) the location of the pressure sensors, (b) the pixel intensities in the image and (c) pixel intensity along the cross-shore measurement transect. The (d) predicted breaking is shown as the percentage of time where pressure was taken hydrostatic because of the presence of a breaking wave or bore.

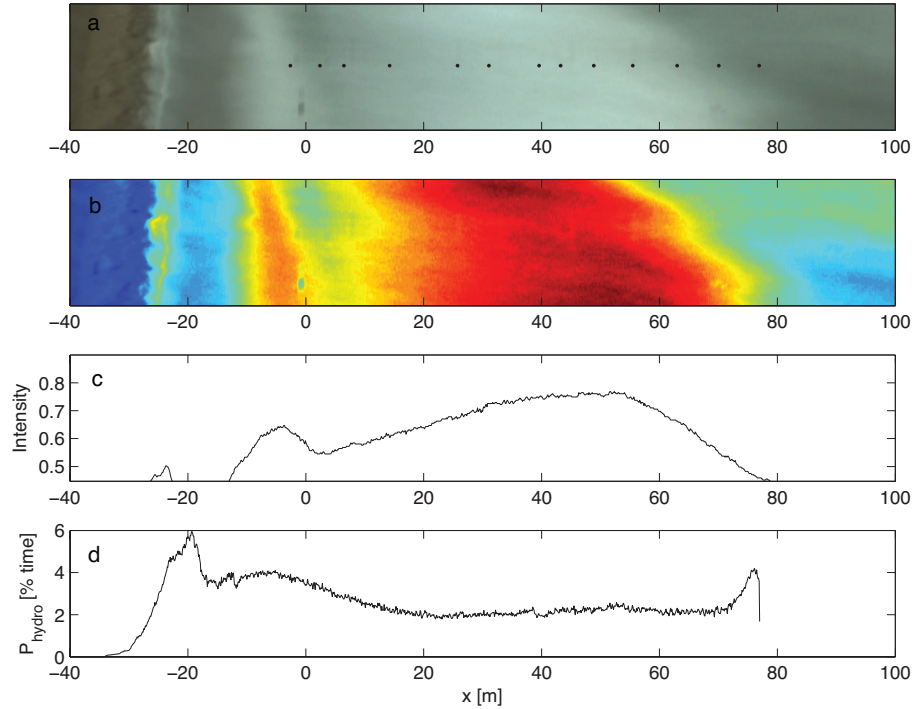


Figure 21: Case 6 - Observed and predicted wave breaking along the cross-shore transect. The extraction of wave breaking from the time-exposure images is shown as, (a) the original time-exposure image with (black dots) the location of the pressure sensors, (b) the pixel intensities in the image and (c) pixel intensity along the cross-shore measurement transect. The (d) predicted breaking is shown as the percentage of time where pressure was taken hydrostatic because of the presence of a breaking wave or bore.

beach face is with 0.1 steeper than the others. This results in a stabilization of the wave height shoreward of the sandbar crest and relatively high waves close to the shore.

The predicted HF  $H_{m0}$  shows overall good agreement with the observations, reflected by the low rms error values per case (Table 2). The error decreases towards shore, but increases again in very shallow water (Figure 23). In deeper water the wave height is often under-predicted, in shallow water over-predicted (Figure 24). The error at the seaward side is partly explained by boundary effects of the non-hydrostatic pressure (see also Section 3.5.4). The HF  $H_{m0}$  of the data measured by the pressure sensor fixed to the ADV frame, does not fit in the cross-shore trend. It seems slightly too low for all cases, this explains the slight under-prediction of  $H_{m0}$  at  $x \approx 63 - 40\text{m}$ .

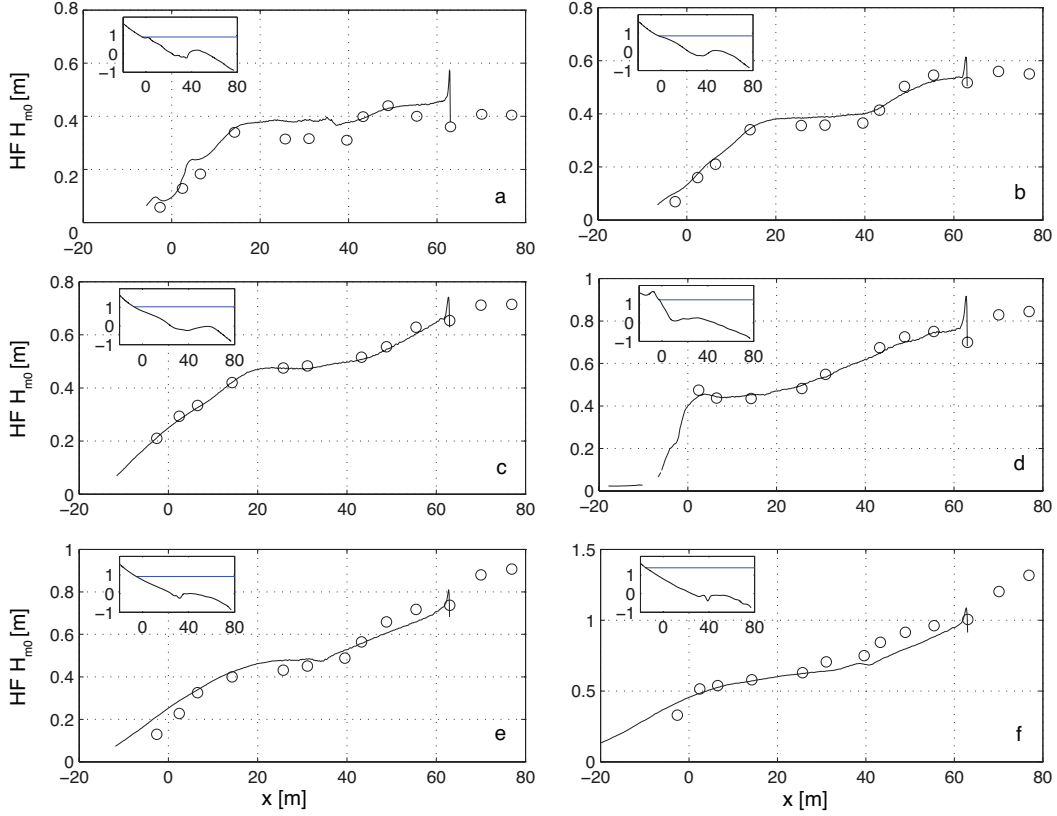


Figure 22: High frequency  $H_{m0}$  predictions (solid line) and observations ( $\circ$ ) for case (a) 1 - (f) 6. The insets show the bottom profile for each case, with cross-shore distance and bottomheight at the x and y-axis respectively.

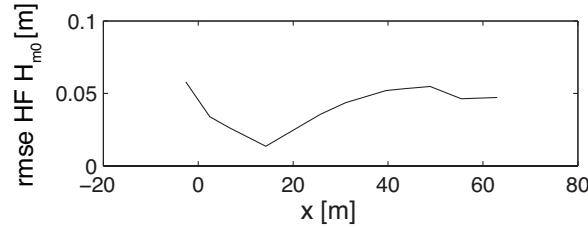


Figure 23: Cross-shore rms error for predicted high-frequency wave height for all cases combined.



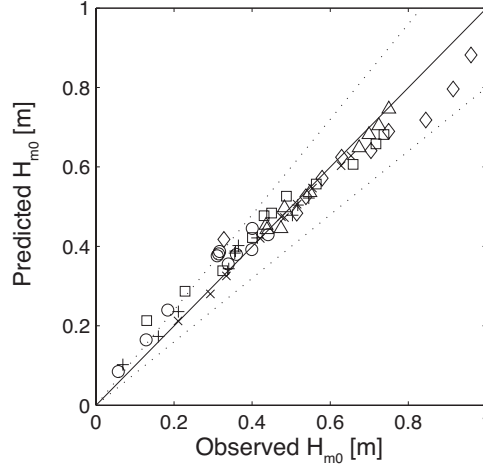


Figure 24: Predictions of high frequency  $H_{m0}$  versus observations for cases ( $\circ$ ) 1, (+) 2, ( $\times$ ) 3, ( $\triangle$ ) 4, ( $\square$ ) 5 and ( $\diamond$ ) 6. The solid line represents perfect agreement, dotted lines the 20% difference.

### 4.3 Wave energy spectra

Wave energy spectra of the observed time-series are shown for four locations ( $x = 76.9, 55.4, 43.2$  and  $14.2\text{m}$ ) per case (Figure 25). These locations are chosen because they represent ( $x = 76.9\text{m}$ ) the most seaward sensor, ( $x = 55.4\text{m}$ ) the crest (or slightly seaward) of the sandbar, ( $x = 43.2\text{m}$ ) the crest (or slightly shoreward) of the sandbar and ( $x = 14.2\text{m}$ ) the beach face. These observed wave spectra are compared with the predictions per case (Figure 26) and the evolution of the wave spectra is discussed using observed (Figures 27 - 32) and predicted (Figure 33) bispectra.

- **Case 1** shows a bimodal spectra, with a swell- ( $f \sim 0.07\text{Hz}$ ) and wind-wave ( $f \sim 0.2 - 0.4\text{Hz}$ ) peak (Figure 25a). In the shoaling zone, energy-density at  $f \sim 0.13\text{Hz}$  increases, especially above the seaward toe of the sandbar (between  $x = 76.9 - 55.4\text{m}$ ), above the crest of the sandbar also an increase of energy-density in the surrounding frequencies ( $0.1 - 0.2\text{Hz}$ ) is visible. Energy-density in the wind-wave frequencies decreases due to wave breaking.

The predicted energy-density (Figure 26) is similar to the observations, the increase at  $f \sim 0.13\text{Hz}$  is also present, but over-predicted. The over-prediction in this frequency might be explained by the predicted bicoherence values for the self-self wave interaction of  $f \sim 0.06\text{Hz}$  ( $b(0.06, 0.06) = 0.28$  at  $x = 43.2\text{m}$ ) above the seaward slope and crest of the sandbar (Figure 33), this indicates more energy is transferred to twice the frequency in comparison with the observations (Figure 27). The predicted energy-density at very low frequencies increases throughout the profile, in contrary to the observations.

- **Case 2** consists of mild-energetic swell, with a peak frequency of  $0.08\text{Hz}$  (Figure 25b). For the high frequencies ( $f > 0.05\text{Hz}$ ), the energy-density decreases for  $f < 0.35\text{Hz}$  and slightly increases for  $f > 0.35\text{Hz}$ . The increase in energy-density in the higher frequencies is also clearly visible in the time series and in a snapshot of the wave field (Figure 35). After breaking, small waves appear in the troughs of the relatively long swell waves. The time series are further explained in Section 4.4 to discuss the shape of the waves.

The increase in energy-density at higher frequencies can be attributed to non-linear energy coupling between frequencies in the range  $f = 0.09 - 0.21\text{Hz}$  (Figure 28). The particular increase at  $f \sim 0.36\text{Hz}$  between  $x = 63.0 - 55.4\text{m}$  is probably caused by coupling between  $f \sim 0.15$  and  $f \sim 0.21\text{Hz}$  ( $b(0.15, 0.21) = 0.47$  at  $x = 63.0\text{m}$ ).

The predictions are in agreement with observations and show both the decrease of energy-density for  $f < 0.35\text{Hz}$  and increase for  $f > 0.35\text{Hz}$  (Figure 26). The energy-density

at very low frequencies is over-predicted from the crest of the sandbar till shore. The predicted values of bicoherence show very close resemblance with the observations, with self-self wave interaction at the peak frequency ( $f \sim 0.09\text{Hz}$ ) throughout the profile, coupling of the peak frequency with  $f \sim 0.15\text{Hz}$  ( $b(0.09, 0.15) = 0.43$  at  $x = 55.4$ ) and a self-self wave interaction at  $f \sim 0.15\text{Hz}$  ( $b(0.15, 0.15) = 0.41$  at  $x = 48.9\text{m}$ ) (Figure 33).

- **Case 3** shows similar trends (Figure 25c), though the development of higher frequency waves was, in comparison with case 2, not as clear in the time series and snapshots.

The bicoherence shows interactions of the primary frequency ( $f \sim 0.12 - 0.15\text{Hz}$ ) with  $f \sim 0.15$ ,  $f \sim 0.21$ ,  $f \sim 0.32$ ,  $f \sim 0.41$  and  $f \sim 0.53\text{Hz}$  (Figure 29). At the most seaward sensor the primary frequency is coupled with the first three frequencies, this extends to the higher frequencies while the waves shoal over the sandbar, until the primary frequency is also coupled with  $f \sim 0.53\text{Hz}$  at the location of wave breaking ( $b(0.12, 0.53) = 0.49$  at  $x = 55.4\text{m}$ ). The high bicoherence levels at the peak frequency ( $b(0.15, 0.15) = 0.59$ ) at the most seaward sensor, indicates a self-self wave interaction coupled to energy at  $f \sim 0.30\text{Hz}$  and explains the reason for the high energy-density at this frequency.

The simulations show too much dissipation at the frequencies  $f \sim 0.12$ ,  $0.18$  and  $0.3\text{Hz}$  around the crest of the sandbar (Figure 26). The predicted bicoherence is, in comparison with the observations, indicates stronger coupling within the peak (Figure 33), but weaker coupling between the peak and higher frequencies.

- **Case 4** The distinct peak frequency at  $f \sim 0.18\text{Hz}$  characterizes case 4 (Figure 25d). The bicoherence values (Figure 30) indicate strong coupling within the peak frequency (up to  $0.83$  at  $x = 48.9\text{m}$ ) and coupling with higher harmonics ( $f \sim 0.35$ ,  $0.53\text{Hz}$ ) while the waves shoal. Bicoherence also indicates nonlinear coupling within the first harmonic ( $f \sim 0.35\text{Hz}$ ) in the shoaling zone, between  $x = 63.0 - 43.2\text{m}$ . The predicted coupling within the peak frequency and between its higher harmonics is weaker than observed, but occurs for the same frequencies (Figure 33). Predicted wave energy-density is very similar to the observed values, only low-frequency energy-density is over-predicted (Figure 26).
- **Case 5** consists of a typical wind wave spectrum (Figure 25e), with no distinct peak frequency. Besides minor differences, predicted wave spectra are in close agreement with observations (Figure 26). The predicted bicoherence values indicate the strongest coupling between  $f \sim 0.12$  and  $f \sim 0.15\text{Hz}$  above the sandbar (Figure 33). This coupling is not found in the observations, but because of the broad spectrum and the fact that the whole section is located in the surf zone, many weak couplings are indicated by the bicoherence (Figure 31).
- **Case 6**, the high-energetic case, shows dissipation for almost all frequencies throughout the transect (Figure 25f). Above the flat crest of the intertidal sandbar, dissipation is present but less pronounced as seaward and landward of this location. The model predicts more dissipation above the sandbar crest, but the predicted spectra are in general close to the observations (Figure 26).

Bicoherence values decrease in landward direction (Figure 32), as the whole transect is located in the surf zone. At the most seaward location, bicoherence values indicate nonlinear coupling within the peak frequency, between the peak frequency ( $f \sim 0.15\text{Hz}$ ) and higher harmonics ( $f \sim 0.29$ ,  $0.44$ ,  $0.59\text{Hz}$ ) and within the first harmonic ( $b(0.29, 0.29) = 0.79$  at  $x = 76.9\text{m}$ ). The predicted bicoherence values indicate the same coupled frequencies above the sandbar, only slightly weaker (Figure 33).

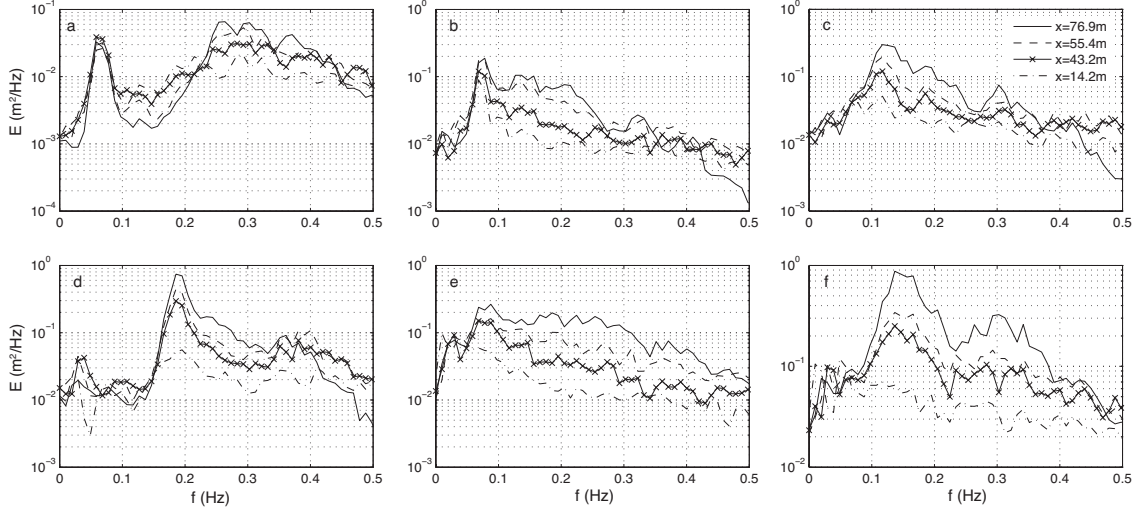


Figure 25: Wave energy spectra of the sea surface elevation time-series for case (a) 1 - (f) 6. Observations at four locations are shown,  $x=76.9, 55.4, 43.2$  and  $14.2$ m.

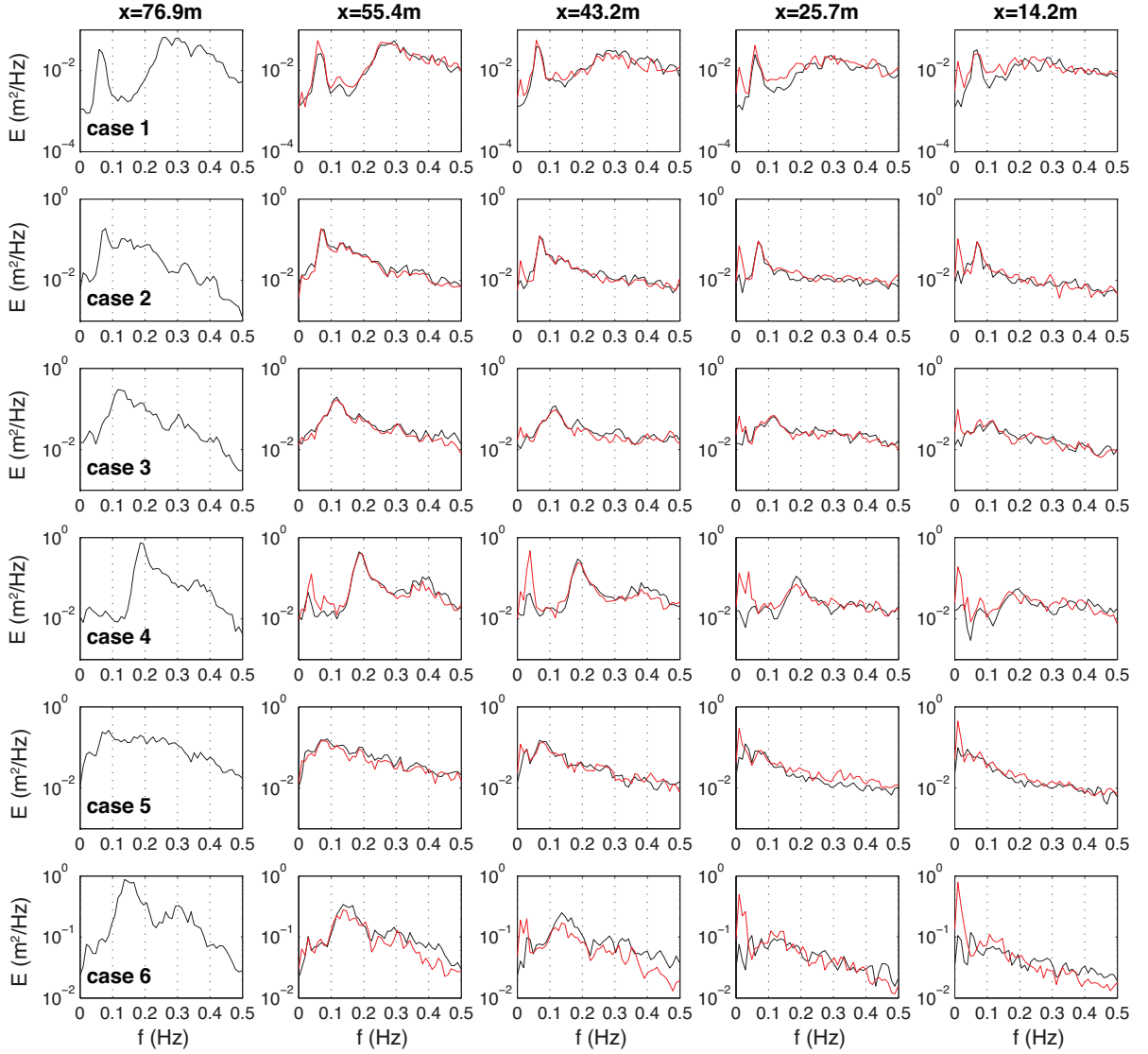


Figure 26: (black) Observed and (red) predicted wave energy spectra per case for 5 measurement locations, from left to right,  $x=76.9, 55.4, 43.2, 25.7$  and  $14.2$ m. The cases 1-6 are shown from top to bottom.

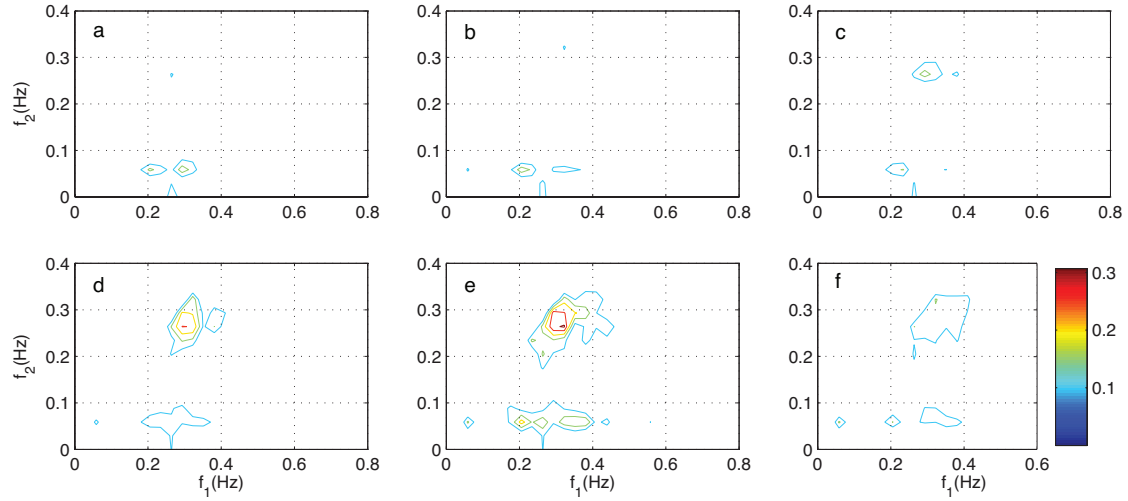


Figure 27: The bicoherence at (a)  $x = 76.9$ , (b)  $70.0$ , (c)  $63.0$ , (d)  $55.4$ , (e)  $48.9$  and (f)  $43.2$  m for case 1. Contour lines are colored (see colorbar), start at 0.1 and are drawn with an interval of 0.05.

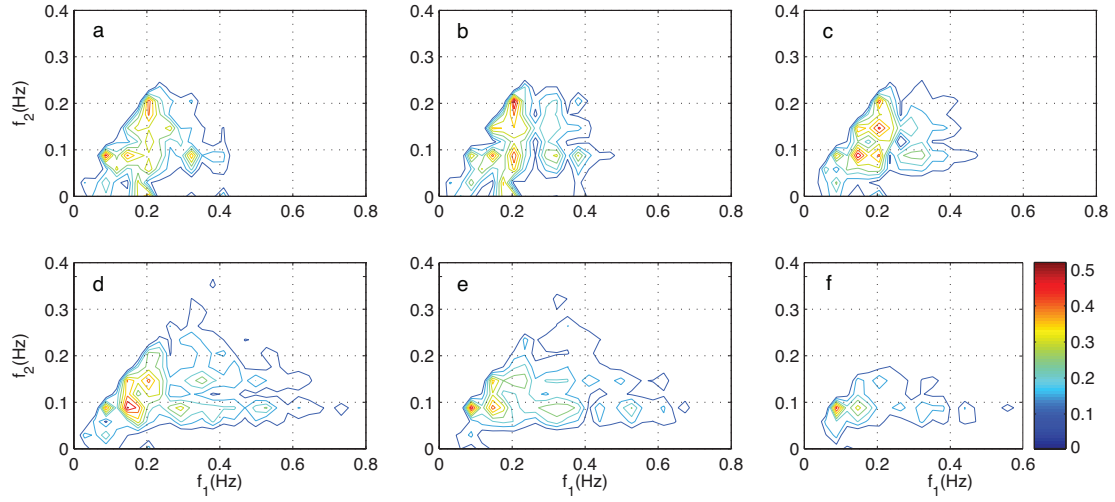


Figure 28: The bicoherence at (a)  $x = 76.9$ , (b)  $70.0$ , (c)  $63.0$ , (d)  $55.4$ , (e)  $48.9$  and (f)  $43.2$  m for case 2. Contour lines are colored (see colorbar), start at 0.1 and are drawn with an interval of 0.05.

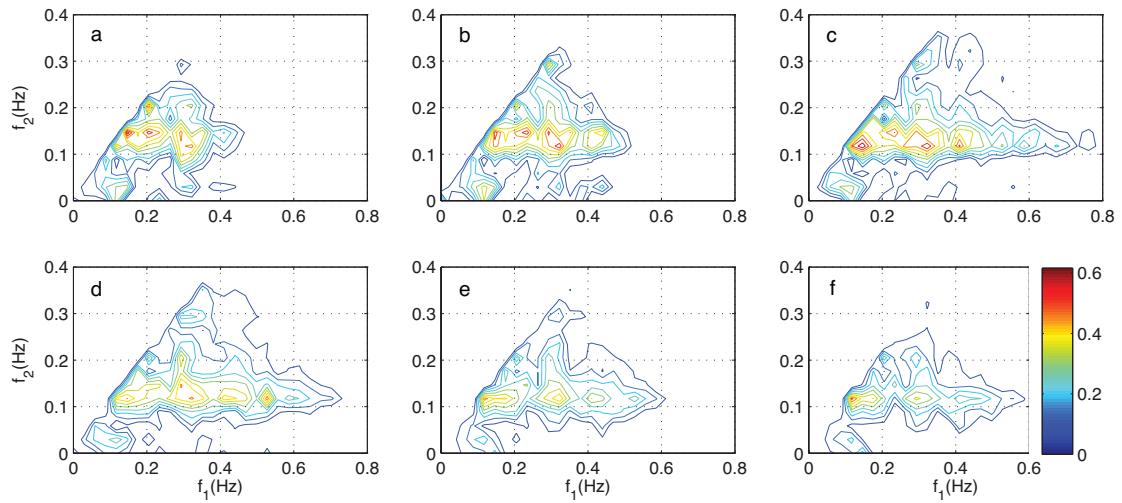


Figure 29: The bicoherence at (a)  $x = 76.9$ , (b)  $70.0$ , (c)  $63.0$ , (d)  $55.4$ , (e)  $48.9$  and (f)  $43.2$  m for case 3. Contour lines are colored (see colorbar), start at 0.1 and are drawn with an interval of 0.05.

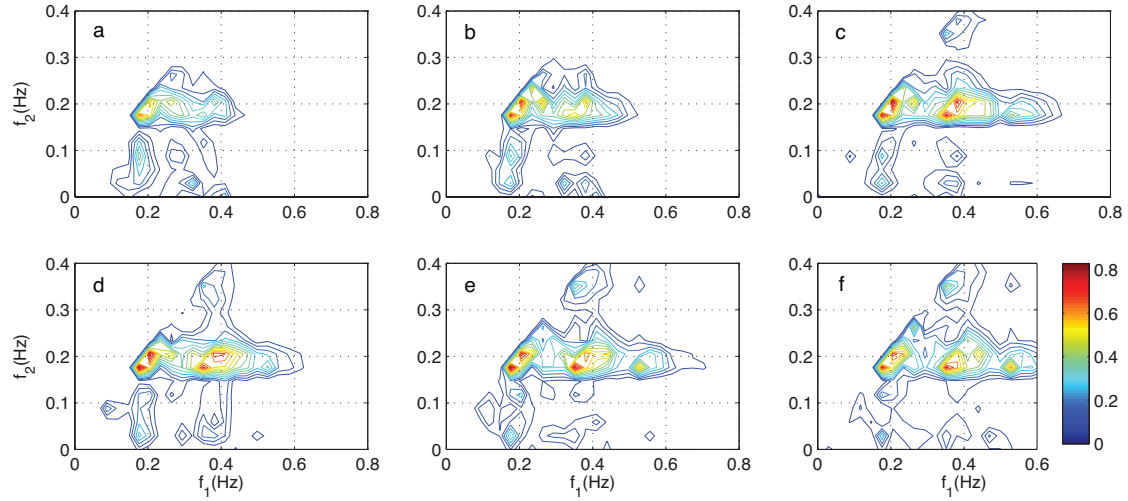


Figure 30: The bicoherence at (a)  $x = 76.9$ , (b)  $70.0$ , (c)  $63.0$ , (d)  $55.4$ , (e)  $48.9$  and (f)  $43.2$ m for case 4. Contour lines are colored (see colorbar), start at  $0.1$  and are drawn with an interval of  $0.05$ .

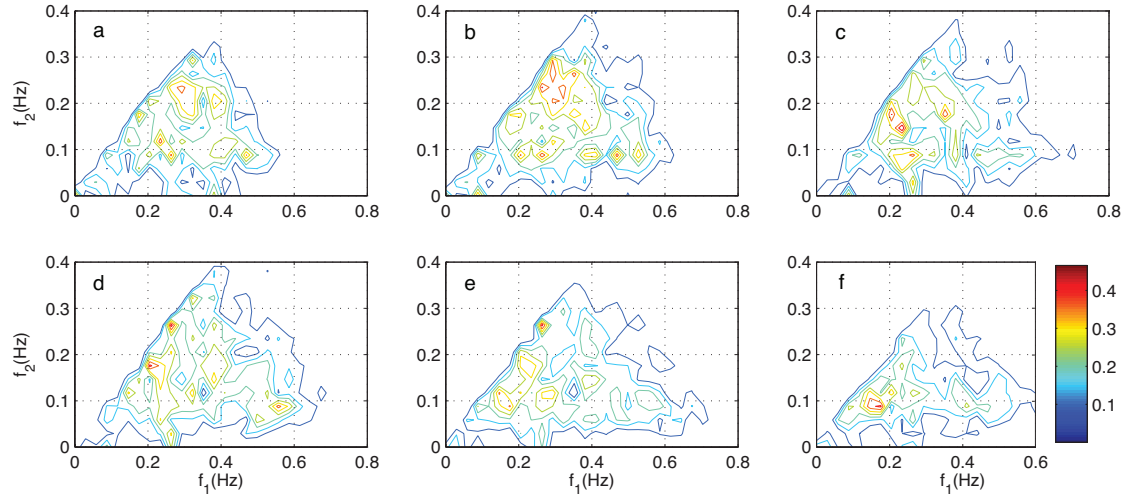


Figure 31: The bicoherence at (a)  $x = 76.9$ , (b)  $70.0$ , (c)  $63.0$ , (d)  $55.4$ , (e)  $48.9$  and (f)  $43.2$ m for case 5. Contour lines are colored (see colorbar), start at  $0.1$  and are drawn with an interval of  $0.05$ .

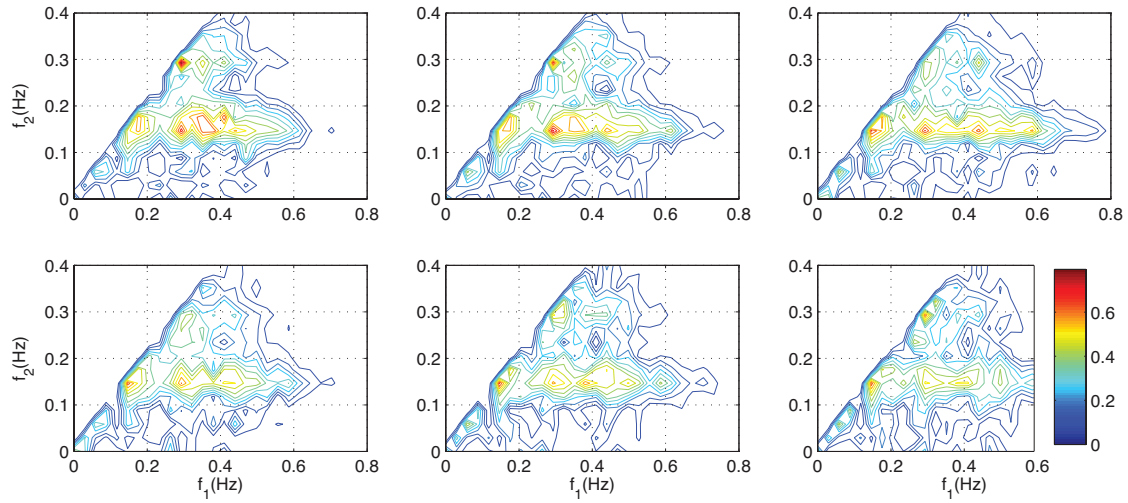


Figure 32: The bicoherence at (a)  $x = 76.9$ , (b)  $70.0$ , (c)  $63.0$ , (d)  $55.4$ , (e)  $48.9$  and (f)  $43.2$ m for case 6. Contour lines are colored (see colorbar), start at  $0.1$  and are drawn with an interval of  $0.05$ .

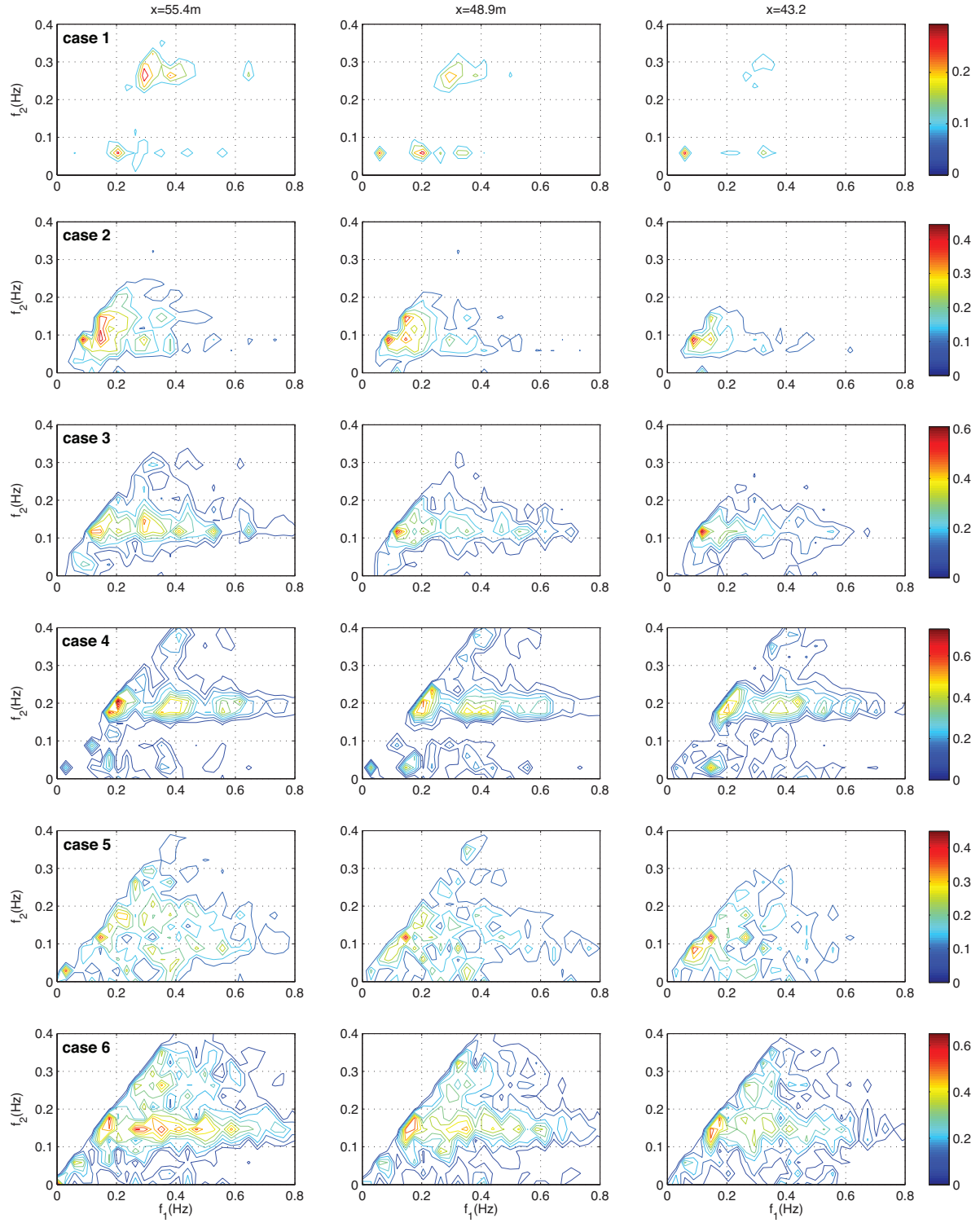


Figure 33: The predicted bicoherence at  $x = 55.4\text{m}$ ,  $x = 48.9\text{m}$  and  $x = 43.2\text{m}$  for all cases. Contour lines are colored (see colorbars), start at 0.1 and are drawn with an interval of 0.05.

#### 4.4 Skewness and Asymmetry

The wave shape evolution in the cross-shore transect is analyzed with the skewness ( $Sk$ ) and asymmetry ( $As$ ) of the time-series. These are calculated as described in Section 3.2.4 and visualized in Figure 36. Note that an increase in  $As$  signifies the number to become more negative, and an increase in  $Sk$  signifies the number to become more positive.

The low-energetic case 1 shows the whole wave shape development, typical for a barred



beach. This makes the case suitable to further explain  $Sk$  and  $As$  in time-series. The wave shape is symmetrical at the most seaward sensor (Figure 34a), with  $Sk \approx 0$  and  $As \approx 0$  (Figure 36). When the waves propagate above the seaward slope of the sandbar, a gradual transformation is visible in the time-series (Figure 34b and 34c) and  $Sk$  and  $As$  increase from 0, at the toe, to  $(-)0.5$ , at the crest of the sandbar. The wave troughs become wider, crests become narrower (increase in  $Sk$ ) and the shoreward wave face becomes steeper than the seaward wave face (increase in  $As$ ). When the wave shape parameters reach their maximum value above the crest of the intertidal sandbar, the highest waves break (see Section 4.1). The values for  $Sk$  and  $As$  return to 0 above the trough of the sandbar, as the water becomes deeper and the waves deshoal (Figure 34d). Shoreward of the sandbar trough, the water depth decreases again, which results in wave shoaling and breaking. Seaward of the second breaking zone (see Section 4.1) at  $x = 14.2\text{m}$ , a mix between symmetric, skewed and asymmetric waves is found (Figure 34e).

The second case consists of mild-energetic swell, with a peak period of 12.8s. This wave period, together with a slightly higher wave height, moves the initiation of wave shape evolution further seaward, in comparison with case 1. The value for  $Sk$  is already 0.6 at  $x = 76.9\text{m}$  and remains high until breaking on the beach face. This high value for  $Sk$  is visible in the time-series (Figure 35), but due to the light conditions, the  $Sk$  is also illustrated by the image taken during the field case (Figure 35f). The image and time-series show the troughs between the waves get wider from  $x = 100$  to  $x = 50\text{m}$  and the crests become higher and more asymmetric until the waves break. The local maximum value of  $As$  is reached above the sandbar crest at  $x = 48.9\text{m}$  (Figure 36b). Above the trough of the sandbar,  $As$  decreases as in case 1, but  $Sk$  remains constant until the second breaking zone. In the long trough of the waves, around 5 small waves develop above the sandbar trough. This reduces  $Sk$ , but  $As$  increases rapidly as the waves propagate into more shallow water and break in the second breaking zone.

The cross-shore trend in wave shape parameters for case 1 and 2 show an increase in  $Sk$

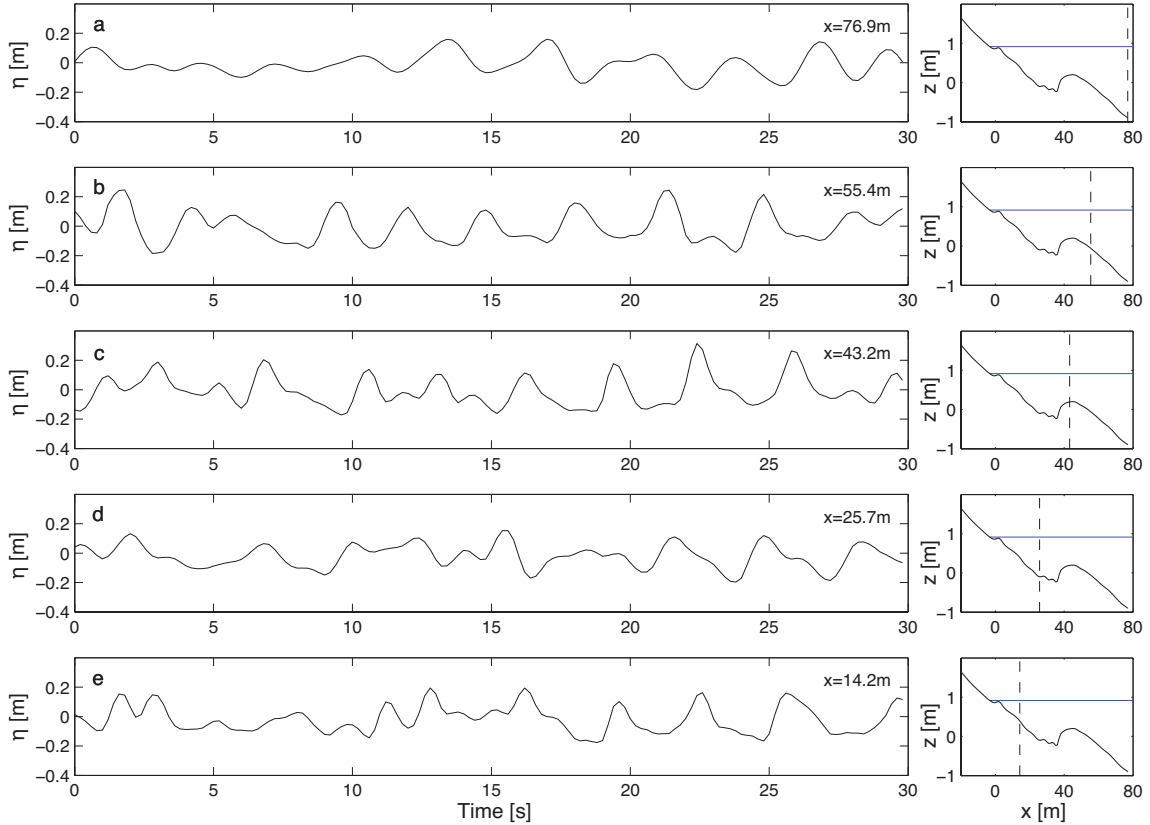


Figure 34: Part of the sea surface time series measured at (a)  $x=76.9$ , (b)  $55.4$ , (c)  $43.2$ , (d)  $25.7$  and (e)  $14.2\text{m}$ , during case 1. The location of each timeseries in respect to the bottom profile is plotted at the right.

and  $As$  in the shoaling zone until waves break above the sandbar crest. Waves de-shoal above the sandbar trough and landward  $As$  increases and  $Sk$  decreases over a short distance until the waves reach the second breaking zone. Close to the shoreline,  $As$  decreases and  $Sk$  increases slightly. Case 3 and 4 show the same dynamics. Case 4 shows a relatively slow transformation of the waves, due to the more shoreward located bar crest, a mild slope seaward of the crest and a relatively high water level.

The higher energetic conditions 5 and 6 do not show the whole trend observed in the low and mid energetic cases, because wave breaking already occurs seaward of the studied transect. For this reason, waves are already skewed and asymmetric at the most seaward sensor. The value of  $As$  reaches a local maximum above the sandbar crest, the effect of de-shoaling above the trough is much smaller, also because the bottom height difference between the crest and the trough of the sandbar is less profound for the high-energetic cases.

The predictions of  $Sk$  and  $As$  for the first three cases show the same trend as the observations (Figure 36). For case 1,  $Sk$  is over-predicted throughout the transect, which could be linked with the over-prediction of energy transfers between frequencies in the shoaling zone (Section 4.3). Case 3 gives the best performance, with an error of 0.10 for both  $Sk$  and  $As$  (Table 3).

The predictions of  $Sk$  for the higher energetic cases 4, 5 and 6 show values comparable

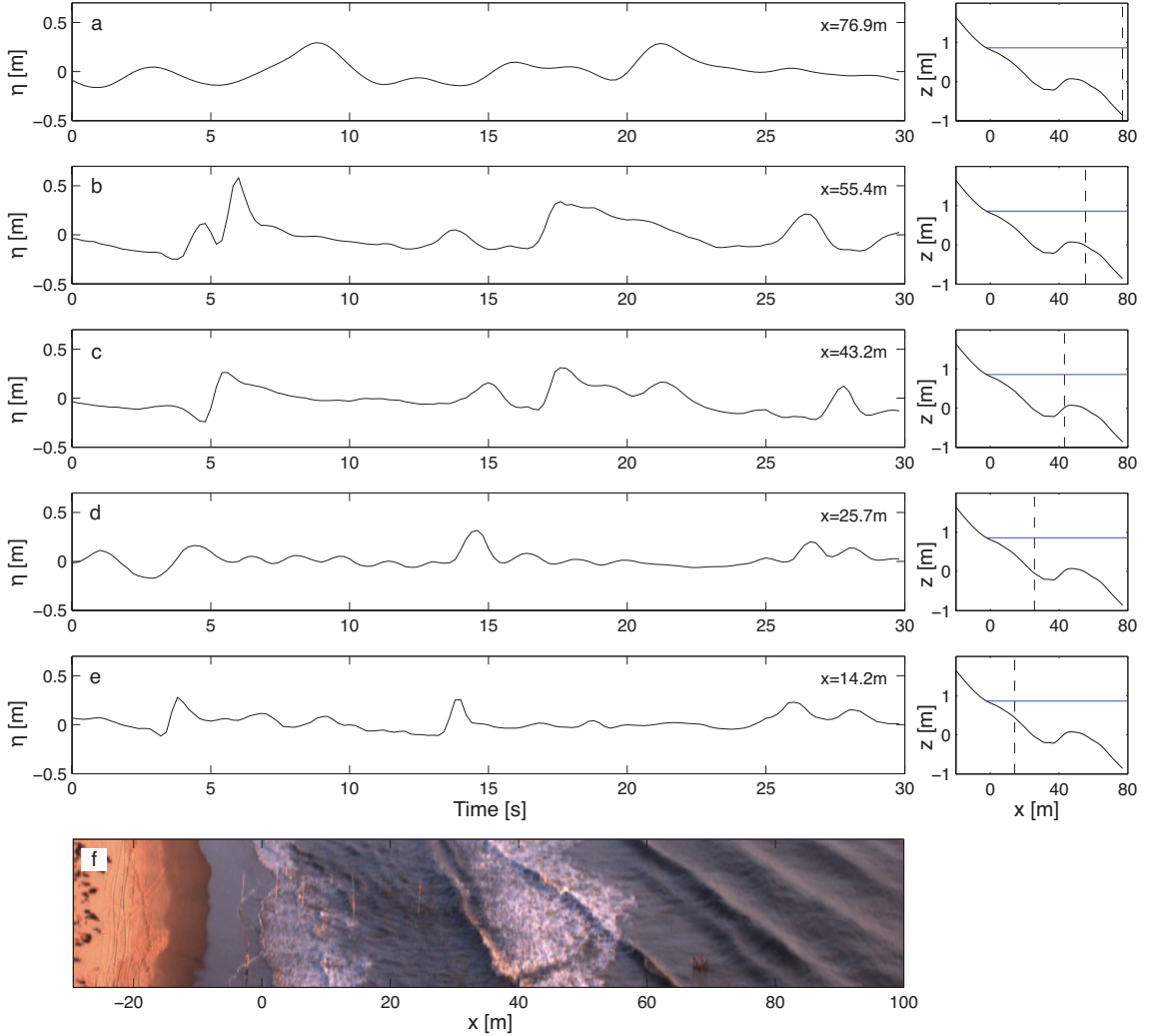


Figure 35: Part of the sea surface time series measured at (a)  $x=76.9$ , (b)  $55.4$ , (c)  $43.2$ , (d)  $25.7$  and (e)  $14.2$ m and (f) a snapshot of the wave field, during case 2. The snapshot is taken from an oblique angle, so the  $x$  axis is only valid along the measurement transect. The location of each timeseries in respect to the bottom profile is plotted at the right.



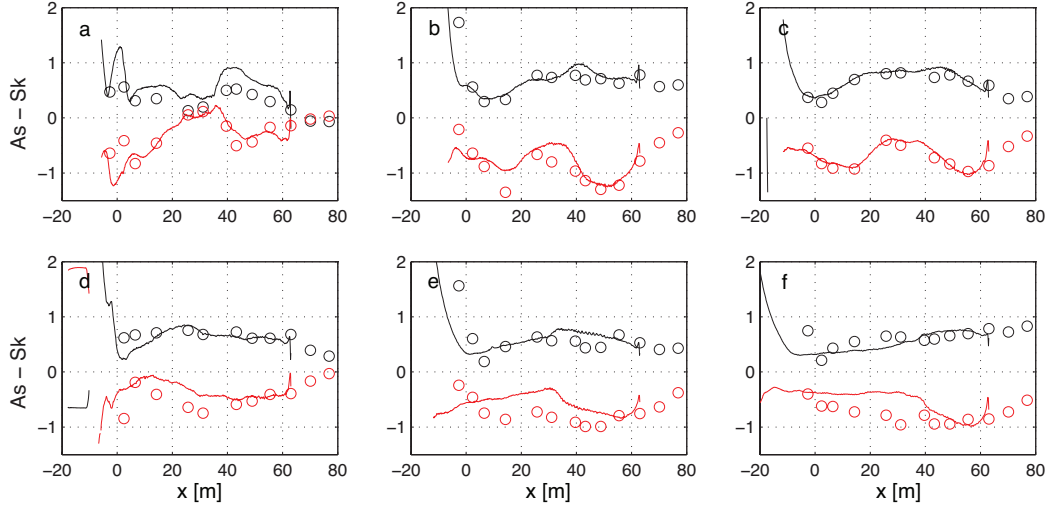


Figure 36: Observed ( $\circ$ ) and (solid line) predicted (black)  $Sk$  and (red)  $As$  for case (a) 1 - (f) 6.

with observations, throughout the transect. Close to the shoreline, in very shallow waters, discrepancies between observed and predicted  $Sk$  are present, this might be due to higher uncertainties in the calculations in very shallow water. The cross-shore rms error for  $Sk$  over all cases quantifies this, with values  $< 0.25$  up to  $x \approx 0$  m and an increase to 0.71 at the location of the most landward sensor (Figure 37a). The predicted  $As$  of the high-energetic cases does show a different trend in comparison to observations, in general an under-prediction of  $As$  is seen landward of the sandbar crest. This results in an rms error for  $As$  around 0.3 for these cases (Table 3).

For both  $Sk$  and  $As$  a local error maximum is found around the location of the sandbar, at  $x \approx 40$  and  $x \approx 30$  m respectively (Figure 37). The location  $x \approx 40$  m represents for most cases the crest of the bar or slightly landward,  $Sk$  is over-predicted at this location for all cases except case 4. Case 4 does show a minor over-prediction at  $x \approx 25$  m, the location of the sandbar crest for this case. The location  $x \approx 30$  m represents the trough of the sandbar, where  $As$  is under-predicted for most cases (Figure 36).

Wave shape parameters  $As$  and  $Sk$  are not consistently under- or over-predicted, but scatter around perfect agreement between predictions and observations is present (Figure 38). In particular the values for  $Sk$  seem randomly distributed around the line of agreement, but this is also caused by the relatively small range of  $Sk$  values found. Predicted values for  $As$  show good agreement with the observations at the extremes, this can be explained by the fact that

Table 3: Rms error for the predicted skewness and asymmetry per case.

Cases	1	2	3	4	5	6
$Sk$ rms error	0.29	0.36	0.10	0.20	0.37	0.18
$As$ rms error	0.23	0.22	0.10	0.27	0.30	0.28

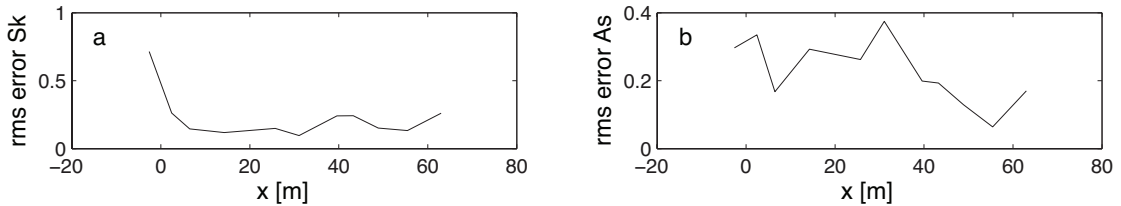


Figure 37: Cross-shore rms error for predicted (a) skewness and (b) asymmetry for all cases combined.

these values occur in the low-energetic cases, where errors for  $As$  predictions are low. The under-prediction of  $As$  in the observed range  $As \approx 0.5 - 1.0$  is caused by the high-energetic cases.

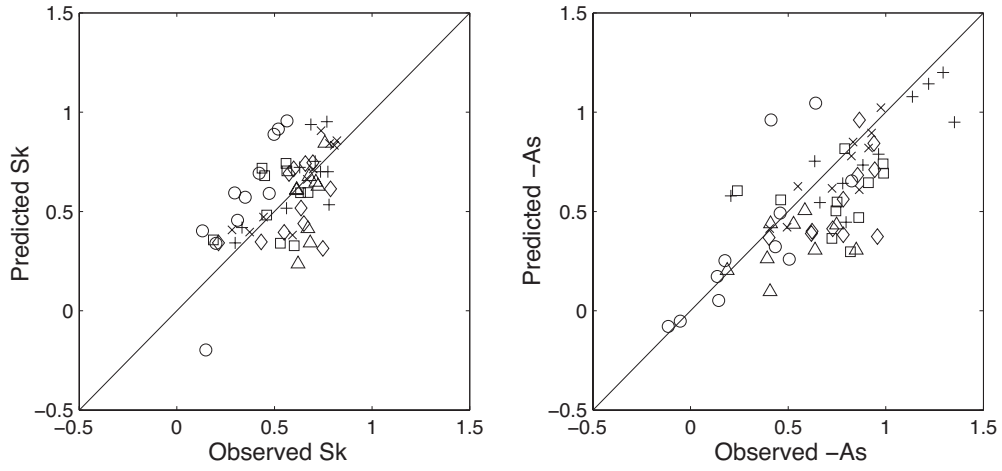


Figure 38: Predictions of  $Sk$  and  $As$  versus observations for cases ( $\circ$ ) 1, ( $+$ ) 2, ( $\times$ ) 3, ( $\triangle$ ) 4, ( $\square$ ) 5 and ( $\diamond$ ) 6. The solid line represents perfect agreement between predictions and observations.

## 5 Conclusions

This study is the first to compare a field measurement dataset, including a wide range of energetic conditions, with simulations by the SWASH model. The capability of the recently developed model to predict the wave breaking location, high frequency wave height, energy-density, skewness and asymmetry of waves propagating over an intertidal sandbar is shown. High frequency wave heights and thereby the amount and location of breaking dissipation are satisfactory predicted by the SWASH model for a wide range of energetic conditions. Hence the hydrostatic pressure assumption at the front face of breaking waves results in a correct amount and location of breaking dissipation. The low frequency wave height is over-predicted up to a factor 2, this is due to the one-dimensional domain, in which directional spread is not included. Due to the lack of directional spread in the short waves, energy is more efficiently transferred to low frequencies.

Prediction of wave shape parameters  $As$  and  $Sk$  are in good agreement with observations for mid-energetic conditions. For high-energetic conditions, especially  $As$  is under-predicted in the surf zone, this might be due to the already high nonlinearity of the time-series used at the seaward boundary, as the outer boundary of the surf zone is located outside of the model domain. The predicted wave shape shows slightly higher error values around the location of the intertidal sandbar.

The wave energy spectra of the predictions and observations are very similar, except for the low-frequencies, where the energy-density is consistently over-predicted. The bicoherence of the bispectra, indicating non-linear energy transfers between frequencies, also show close resemblance for all cases. The bicoherence is also important for the wave shape, as it quantifies which frequency pairs contribute to the development of  $As$  and  $Sk$ .

Boundary effects in the model predictions are due to the lack of non-hydrostatic pressure at the boundary, proven by the absence of boundary effects when only hydrostatic pressure is included in the simulations. A distance of 20-30m is needed to overcome those effects, which is a substantial part of the 80m long transect. Including only hydrostatic pressure reduces the accuracy of the predictions though, as waves tend to over-steepen, resulting in higher values for  $As$  and as a result also more wave breaking dissipation.

## 6 Discussion and Recommendations

Modeling hydrodynamics in the nearshore zone requires a good representation of the incoming waves at the seaward boundary. In the ideal case, those are measurements taken in deep water and filtered for shoreward propagating waves. In the current research a large part of the discrepancies in the wave shape are due to high nonlinearities at the seaward boundary, especially for high-energetic conditions. For further measurement campaigns including high-energetic conditions, it would be useful to obtain sea surface and velocity measurements further offshore.

The one-dimensional simulations performed during this study, showed already good agreement with observations. But the infragravity-wave height is over-predicted with factor two, caused by the lack of directional spreading. The directional spread also influences wave nonlinearity. It is therefore expected that the accuracy of low frequency energy will increase when a two-dimensional domain is used, this will also further increase the accuracy of the nonlinearity of the waves.

The linear interpolation in time of instrument heights and bottom profiles could result in errors in the final results. Low tide periods are included in those interpolations, while during low tide bottom profile and instrument height do not change. The instrument height is important for the water depth and also influences the correction of measured pressure to sea surface elevation. Measured and interpolated bottom profiles are used in the simulations and minor differences

will result in a small error.

All simulations are performed with one vertical layer, more layers are especially needed for the representation of wave dispersion, which is not as important in shallow waters. Although it is expected that predictions for low frequency energy will also improve with a higher vertical resolution. Unfortunately for reasons of model instability and efficiency, simulations with two layers were not feasible during this study.

## References

- Battjes, J. A., Janssen, J., 1978. Energy loss and set-up due to breaking of random waves. Proc. 16th Int. Conf. on Coastal Engineering, ASCE, New York, 570–587.
- Brinkkemper, J. A., 2012. Modeling and parameterization of wave run-up on beaches in Yucatan, Mexico, internship report, LIPC, Universidad Nacional Autónoma de México and University Utrecht.
- Casulli, V., 1999. A semi-implicit finite difference method for non-hydrostatic, free-surface flows. Int. J. Numer. Meth. Fluids 30, 425–440.
- Casulli, V., Stelling, G. S., 1998. Numerical simulation of 3d quasi-hydrostatic, free-surface flows. J. Hydr. Engrg. 124, 678–686.
- Cornish, V., 1898. On sea beaches and sand banks. Geology 2, 628–674.
- Doering, J. C., Bowen, A. J., 1995. Parametrization of orbital velocity asymmetries of shoaling and breaking waves using bispectral analysis. Coastal Engineering 26, 15–33.
- Elgar, S., Guza, R. T., 1985. Observations of bispectra of shoaling surface gravity waves. Journal of Fluid Mechanics 161, 425–448.
- Elgar, S., Guza, R. T., 1986. Nonlinear model predictions of bispectra of shoaling surface gravity waves. Journal of Fluid Mechanics 167, 1–18.
- Guza, R., Thornton, E. B., 1980. Local and shoaled comparisons of sea surface elevations, pressures, and velocities. Journal of geophysical research 85 (C3), 1524–1530.
- Guza, R. T., Thornton, E. B., Holman, R. A., 1984. Swash on steep and shallow beaches. Proc. 19th Coastal Eng. Conf., 708–723.
- Kim, Y. C., Powers, E. J., 1979. Digital bispectral analysis and its applications to nonlinear wave interactions. IEEE Transactions on Plasma Science 7 (2), 120–131.
- Madsen, P. A., Bingham, H. B., Liu, H., 2002. A new boussinesq method for fully nonlinear waves from shallow to deep water. Journal of Fluid Mechanics 462, 1–30.
- Masselink, G., Hughes, M. G., 2003. Introduction to Coastal Processes & Geomorphology. Hodder Education.
- Musumeci, R. E., Svendsen, I. A., Veeramony, J., 2005. The flow in the surf zone: a fully nonlinear boussinesq-type of approach. Coastal Engineering 52, 565–598.
- Peregrine, D. H., 1967. Long waves on a beach. Journal of Fluid Mechanics 27, 815–827.
- Price, T., Ruessink, B., 2008. Morphodynamic zone variability on a microtidal barred beach. Marine Geology 251, 98–109.
- Raubenheimer, B., Guza, R. T., Elgar, S., 1996. Wave transformation across the inner surf zone. Journal of geophysical research 101 (C10), 25,589–25,597.
- Ribberink, J. S., van der Werf, J. J., O’Donoghue, T., Hassan, W. N., 2008. Sand motion induced by oscillatory flows: Sheet flow and vortex ripples. Journal of Turbulence 9 (N20).
- Ruessink, B. G., Kuriyama, Y., Reniers, A. J. H. M., Roelvink, J. A., Walstra, D. J. R., 2007. Modeling cross-shore sandbar behavior on the timescale of weeks. Journal of Geophysical Research 112.
- Ruessink, B. G., Michallet, H., Abreu, T., Sancho, F., der A, D. A. V., der Werf, J. J. V., Silva, P. A., 2011. Observations of velocities, sand concentrations, and fluxes under velocityasymmetric oscillatory flows. Journal of Geophysical Research 116.
- Ruessink, B. G., Ramaekers, G., van Rijn, L. C., 2012. On the parameterization of the free-stream non-linear wave orbital motion in nearshore morphodynamic models. Coastal Engineering 65, 56–63.

- Ruessink, B. G., Walstra, D. J. R., Southgate, H. N., 2003. Calibration and verification of a parametric wave model on barred beaches. *Coastal Engineering* 38, 139–149.
- Sorensen, R. M., 2005. *Basic Coastal Engineering*, 3rd Edition. Springer.
- Stelling, G. S., Zijlema, M., 2003. An accurate and efficient finite-difference algorithm for non-hydrostatic free-surface flow with application to wave propagation. *Int. J. Numer. Meth. Fluids* 43, 1–23.
- Svendsen, I. A., 2006. *Introduction to Nearshore Hydrodynamics*. Vol. 24 of *Advanced Series on Ocean Engineering*. World Scientific.
- van Duin, M., Wiersma, N., Walstra, D., van Rijn, L., Stive, M., 2004. Nourishing the shoreface: observations and hindcasting of the egmond case, the netherlands. *Coastal Engineering* 51, 813–837.
- van Rijn, L., 1990. *Principles of fluid flow and surface waves in rivers, estuaries, seas and oceans*. Aqua publications.
- Wijnberg, K. M., Terwindt, J. H., 1995. Extracting decadal morphological behaviour from high-resolution, long-term bathymetric surveys along the holland coast using eigenfunction analysis. *Marine Geology* 26, 301–330.
- Zijlema, M., Stelling, G. S., 2005. Further experiences with computing non-hydrostatic free-surface flows involving water waves. *Int. J. Numer. Meth. Fluids* 48, 169–197.
- Zijlema, M., Stelling, G. S., 2008. Efficient computation of surf zone waves using the nonlinear shallow water equations with non-hydrostatic pressure. *Coastal Engineering* 55, 780–790.
- Zijlema, M., Stelling, G. S., Smit, P., 2011. SWASH: An operational public domain code for simulating wave fields and rapidly varied flows in coastal waters. *Coastal Engineering* 58 (10), 992–1012.

## A Offshore boundary forcing

Simulations were performed with different offshore boundary conditions; the unfiltered measured time series at OSSI 10, a measured time series at OSSI 10 filtered for only high frequencies ( $f > 0.05Hz$ ) and measured time series at ADV filtered for only incoming waves. The results are shown in Figures 39 and 40. These three simulations are performed with non-hydrostatic pressure included in the computations, as a comparison also one simulations per case has been performed with only hydrostatic pressure.

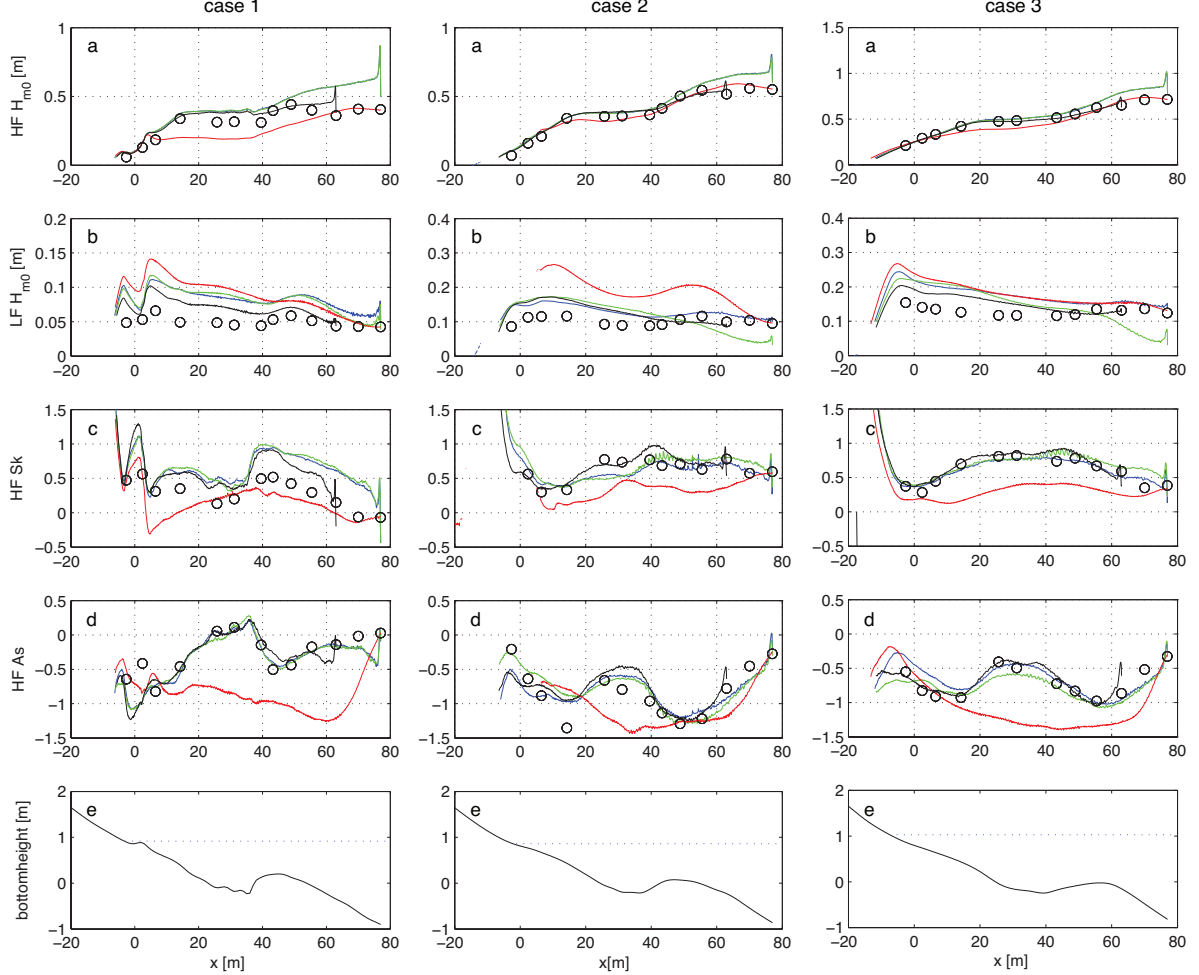


Figure 39: Case 1,2 and 3 - Predicted (a) high frequency wave height, (b) low frequency wave height, (c) high frequency skewness, (d) high frequency asymmetry and (e) the bottom profile with (dotted blue line) still water level. The four lines show the results with as offshore boundary; (blue) unfiltered measured time series at OSSI 10, (green) high frequency filtered measured time series at OSSI 10, (red) unfiltered measured time series at OSSI 10, only hydrostatic computation and (black) time series at ADV filtered for incoming waves.



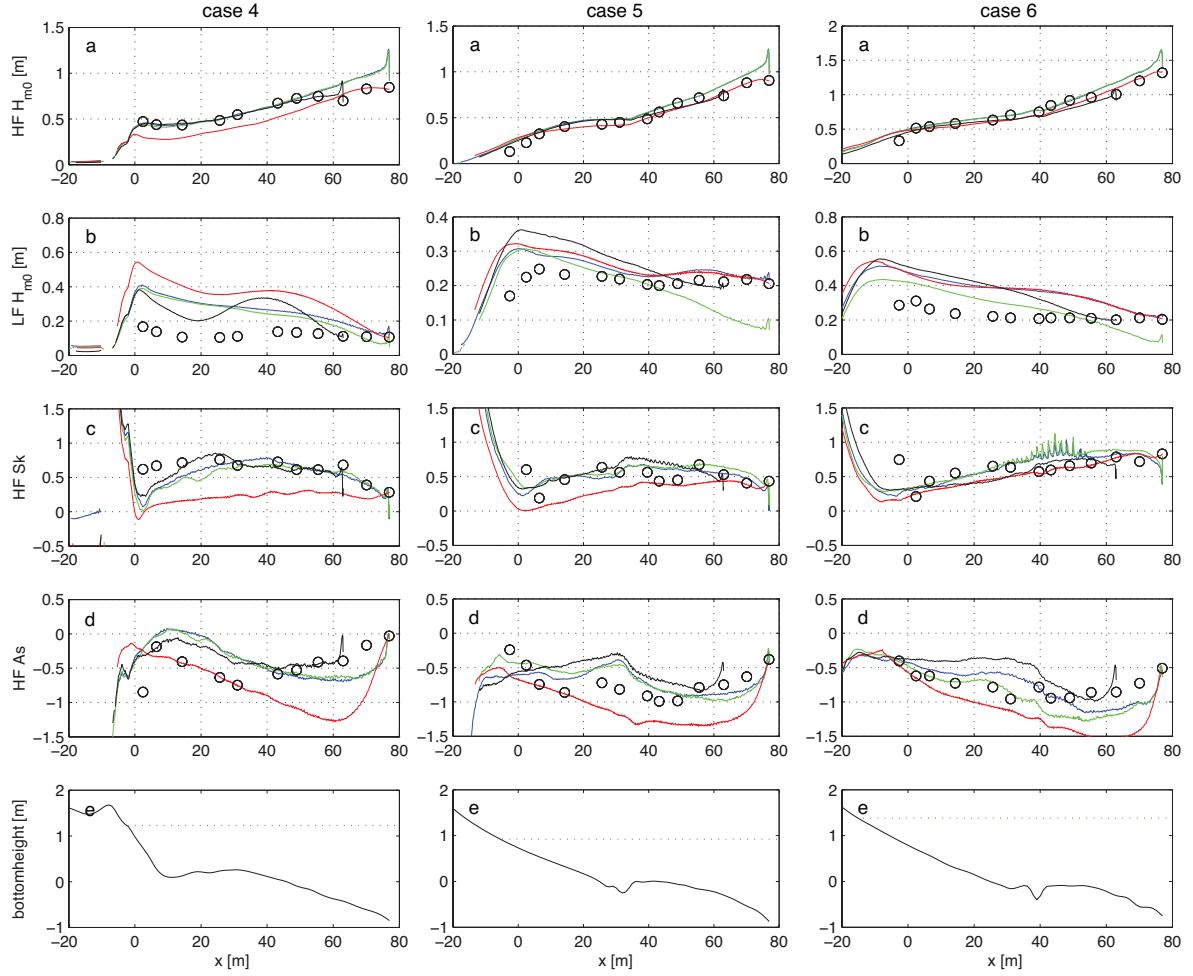


Figure 40: Case 4,5 and 6 - Predicted (a) high frequency wave height, (b) low frequency wave height, (c) high frequency skewness, (d) high frequency asymmetry and (e) the bottom profile with (dotted blue line) still water level. The four lines show the results with as offshore boundary; (blue) unfiltered measured time series at OSSI 10, (green) high frequency filtered measured time series at OSSI 10, (red) unfiltered measure time series at OSSI10, only hydrostatic computation and (black) time series at ADV filtered for incoming waves.